nature biomedical engineering

Article

https://doi.org/10.1038/s41551-024-01258-8

Targeting overexpressed antigens in glioblastoma via CAR T cells with computationally designed high-affinity protein binders

Received: 21 August 2023

Accepted: 5 September 2024

Published online: 17 October 2024

Check for updates

Zhen Xia[1,2,3,4,5], Qihan Jin[1,2,5,6], Zhilin Long[1,2,3,4,5], Yexuan He[5], Fuyi Liu[7], Chengfang Sun[1,8], Jinyang Liao[1,2,5,6], Chun Wang[7], Chentong Wang[1,2,5,6], Jian Zheng[7], Weixi Zhao[1,2,3,4,5], Tianxin Zhang[1,2,5,6], Jeremy N. Rich[9], Yongdeng Zhang[5], Longxing Cao[1,2,5,6] ✉ & Qi Xie[1,2,3,4,5] ✉

Chimeric antigen receptor (CAR) T cells targeting receptors on tumour cells have had limited success in patients with glioblastoma. Here we report the development and therapeutic performance of CAR constructs leveraging protein binders computationally designed de novo to have high affinity for the epidermal growth factor receptor (EGFR) or the tumour-associated antigen CD276, which are overexpressed in glioblastoma. With respect to T cells with a CAR using an antibody-derived single-chain variable fragment as antigen-binding domain, the designed binders on CAR T cells promoted the proliferation of the cells, the secretion of cytotoxic cytokines and their resistance to cell exhaustion, and improved antitumour performance in vitro and in vivo. Moreover, CARs with the binders exhibited higher surface expression and greater resistance to degradation, as indicated by bulk and single-cell transcriptional profiling of the cells. The de novo design of binding domains for specific tumour antigens may potentiate the antitumour efficacy of CAR T cell therapies for other solid cancers.

Glioblastoma is one of the most aggressive and deadly cancers, with a median survival time of approximately 15 months, despite the application of strong therapies, including surgical resection, chemotherapy and radiotherapy[1,2]. Glioblastoma is considered as an immunologically cold tumour with very little T cell infiltration, which limits the effect of immune checkpoint blockade therapy[3–5]. However, adoptive T cell transfer therapies, especially chimeric antigen receptor (CAR) T cell therapy, have shown some early evidence of clinical response, although the overall outcomes are still unsatisfactory[6,7].

CAR therapy has achieved great success in the treatment of haematological malignancies[8–10], but the treatment of solid tumours remains challenging, largely owing to challenges related to CAR T cell tumour infiltration, persistence, expansion and exhaustion, as well as the need to overcome the immunosuppressive tumour microenvironment[11–13]. From the original first-generation CAR construct to the most recent

[1]Westlake Disease Modeling Laboratory, Westlake Laboratory of Life Sciences and Biomedicine, Hangzhou, China. [2]Research Center for Industries of the Future, Westlake University, Hangzhou, China. [3]Key Laboratory of Growth Regulation and Translational Research of Zhejiang Province, School of Life Sciences, Westlake University, Hangzhou, China. [4]Institute of Basic Medical Sciences, Westlake Institute for Advanced Study, Hangzhou, China. [5]School of Life Sciences, Westlake University, Hangzhou, China. [6]Artificial Intelligence Drug Design Core Laboratory, Westlake Laboratory of Life Sciences and Biomedicine, Hangzhou, China. [7]Department of Neurosurgery, The Second Affiliated Hospital of Zhejiang University School of Medicine, Hangzhou, China. [8]School of Medicine, Zhejiang University, Hangzhou, China. [9]University of Pittsburgh Medical Center Hillman Cancer Center, Department of Neurology, University of Pittsburgh, Pittsburgh, PA, USA. ✉e-mail: caolongxing@westlake.edu.cn; xieqi@westlake.edu.cn

fourth-generation CAR construct, substantial efforts have been made to improve CAR design, but the majority have focused on only the intracellular signalling domain[14]. Recently, we and others demonstrated that the combination of a high-throughput CRISPR screening and CRISPR-based gene editing technology potentiated CAR antitumour efficacy[15–17]. However, very few improvements have been made to the extracellular antigen-binding domain, with the vast majority of CAR constructs using a single-chain fragment variable (scFv) derived from a monoclonal antibody.

The scFv fuses the variable regions of the heavy chain (VH) and light chain (VL) of an antibody via a short linker peptide. However, the low folding stabilities of the VH and VL lead to the aggregation or misfolding of the scFv, which may attenuate the on-target effect and cause early exhaustion of CAR T cells[18–23]. To overcome these problems caused by the traditional scFv, we needed a strategy to develop convenient and structurally stable antigen-binding domains for CAR T cells.

Recent advances of computational protein design have enabled the generation of protein binders with predefined targeting site and binding configuration to perform the desired functions[24–27]. The de novo binders can be designed purely in silico with atomic accuracy, and they showed specific binding against their targets, with low nanomolar to picomolar affinities. The de novo binders can overcome many of the biochemical limitations inherent to natural protein-derived binders, such as scFv, owing to their unique biochemical and thermodynamic characteristics: small size, high solubility, extreme stability and high engineerability. Thus, the designed binders offer a way of generating protein-based therapeutics, and some examples include the de novo design of picomolar SARS-CoV-2 virus inhibitors[26], cytokine mimetics[25] and cell signalling modulators[27,28]. We reasoned that de novo binders recognizing tumour-related antigens could also be utilized in the CAR T system to further improve its potency and efficacy.

Herein, we developed a CAR T cell therapy using a de novo-designed binder (DNDB) instead of a typical scFv to target a tumour cell surface antigen. Our DNDB-CAR T cells exhibited improved antitumour efficacy both in vitro and in vivo. Taken together, our study results identified a new approach to design the extracellular antigen-binding domain of CAR T cells with a precise binding configuration and high affinity, providing a potential therapeutic benefit for CAR T cell therapy.

Results

EGFR binder CAR T cells efficiently eliminate glioblastoma cells

Epidermal growth factor receptor (EGFR) is overexpressed in the majority of glioblastomas, making it a promising tumour antigen for CAR T cell therapy. Our previous study documented that a DNDB specifically bound to the EGFR protein with a high binding affinity and blocked the interaction between EGFR and its native ligand EGF[27] (Fig. 1a,b). We further confirmed that the free EGFR binder has low immunogenicity, which is consistent with previous reports[24,25,29] (Extended Data Fig. 1a,b). For the immunogenicity test, we injected mice with 50 μg of purified binder protein, a concentration substantially higher than that expressed on the CAR T cell surface. On the basis of our experiments, we did not detect any anti-binder immunoglobulin G (IgG), indicating a low potential for immunogenicity of our EGFR binder CAR T cells. We then tested whether an EGFR binder could be used for CAR T cell therapy. Thus, we designed a CAR construct incorporating a CD8 signal peptide, an EGFR binder for tumour surface antigen recognition, a CD8α hinge domain, a CD8α transmembrane domain, and intracellular costimulatory domains (4-1BB or CD28) and signalling domains (CD3ζ) (Fig. 1c). We also constructed a traditional scFv CAR, which has been studied in a phase I clinical trial (NCT01869166), as a positive control[30] (Fig. 1c and Extended Data Fig. 1c). Both the binder and scFv have the ability to bind to the actual tumour-associated antigens (Extended Data Fig. 1d). Glioblastoma stem cells (GSCs) are essential in tumorigenesis and resistance to most current therapies, including immunotherapy[31]. Therefore, we evaluated the antitumour activity of these CAR T cells using four GSC lines with high expression of EGFR, namely, GSC3565, MGG4, MGG6 and GSC468 (Fig. 1d). GSCs were cocultured with nontransduced control T cells, EGFR binder CAR T cells or EGFR scFv CAR T cells with the 4-1BB or CD28 costimulatory domain at different effector cell-to-target cell (E:T) ratios. Compared with EGFR scFv CAR T cells, EGFR binder CAR T cells showed stronger killing potency against GSCs, especially at the lower E:T ratio (Fig. 1e and Extended Data Fig. 1e). Using fluorescence imaging, we also found that EGFR binder CAR T cells efficiently eliminated GSCs in a shorter time (Fig. 1f,g). We further confirmed the stronger tumour-killing potency of EGFR binder CAR T cells using primary tumour cells derived from glioblastoma specimens (Fig. 1h,i). Consistent with previous studies, we found that the 4-1BB costimulatory domain performed better than the CD28 costimulatory domain in both scFv and binder CARs. Overall, we developed an EGFR binder CAR T cell product with strong tumour cytotoxicity.

EGFR binder CAR T cells show high specificity and minimal off-target effects

To test whether the antitumour activity of EGFR binder CAR T cells specifically relies on EGFR binding, we created two hydrophobic-to-polar mutations in the EGFR binder interface (F7E and W52E) to disrupt its interaction with EGFR (Fig. 2a,b). These two mutants showed no detectable binding signal in the biolayer interferometry assay (Supplementary Fig. 1a,b). Meanwhile, they completely blocked the tumour-killing activity of EGFR binder CAR T cells in coculture experiments with multiple GSCs at different E:T ratios (Fig. 2c), which strongly indicated the high specificity of the EGFR binder CAR T cells. We next evaluated the off-target effects of EGFR binder CAR T cells. We tested a panel of noncancerous human cells with undetectable EGFR expression (lower than 1%), including human kidney epithelial cells (HEK293T), human induced pluripotent stem cell (iPSC)-derived primary astrocytes, human iPSC-derived neural progenitor cells (iPSC-NPS), the commercially available neural stem-like cell line NSC11, human umbilical vein endothelial cells (HUVECs) and peripheral blood mononuclear cells (PBMCs) (Fig. 2d). EGFR binder CAR T cells did not target any of the tested noncancerous cells in the in vitro cytotoxicity assays (Fig. 2e).

Fig. 1 | EGFR binder CAR T cells enable to glioblastoma cell killing. a, The naturally occurring EGFR protein structure is shown as a surface representation, and the region targeted for the EGFR binder (green) is coloured yellow; the remainder of the target surface is grey. The PDB identifier was 1MOX (EGFR). **b**, Biolayer interferometry characterization of the binding of the EGFR binder to EGFR. Biotinylated EGFR proteins were loaded onto streptavidin (SA) biosensors and incubated with protein binders in solution to measure association and dissociation. Twofold serial dilutions were tested for each binder, and the highest concentration was labelled. The grey curves represent experimental data, and the orange curves represent fit curves. **c**, Diagram of the indicated CAR structures. **d**, EGFR expression on different GSCs was measured by anti-EGFR antibody flow cytometric staining. **e**, Percent tumour cell killing activity of the indicated CAR T cells against cocultured GSCs at different E:T ratios. Data are shown as the mean ± s.d. (ANOVA; NS, not significant; $n = 3$). **f**, Image of the indicated CAR T cells cocultured with mCherry-transduced GSC3565 cells (E:T = 1:4) at different time points. **g**, Quantification of the fluorescence signal intensity (AU) of tumour cells shown in **h**. **h**, EGFR expression on primary glioblastoma cells was measured by EGFR-specific antibody flow cytometric staining. **i**, Percent tumour-killing activity of the indicated CAR T cells against two cocultured primary glioblastoma cell models (12388157 and 12479390) at different E:T ratios. Data are shown as the mean ± s.d. (ANOVA; NS, not significant; $n = 3$).

https://doi.org/10.1038/s41551-024-01258-8

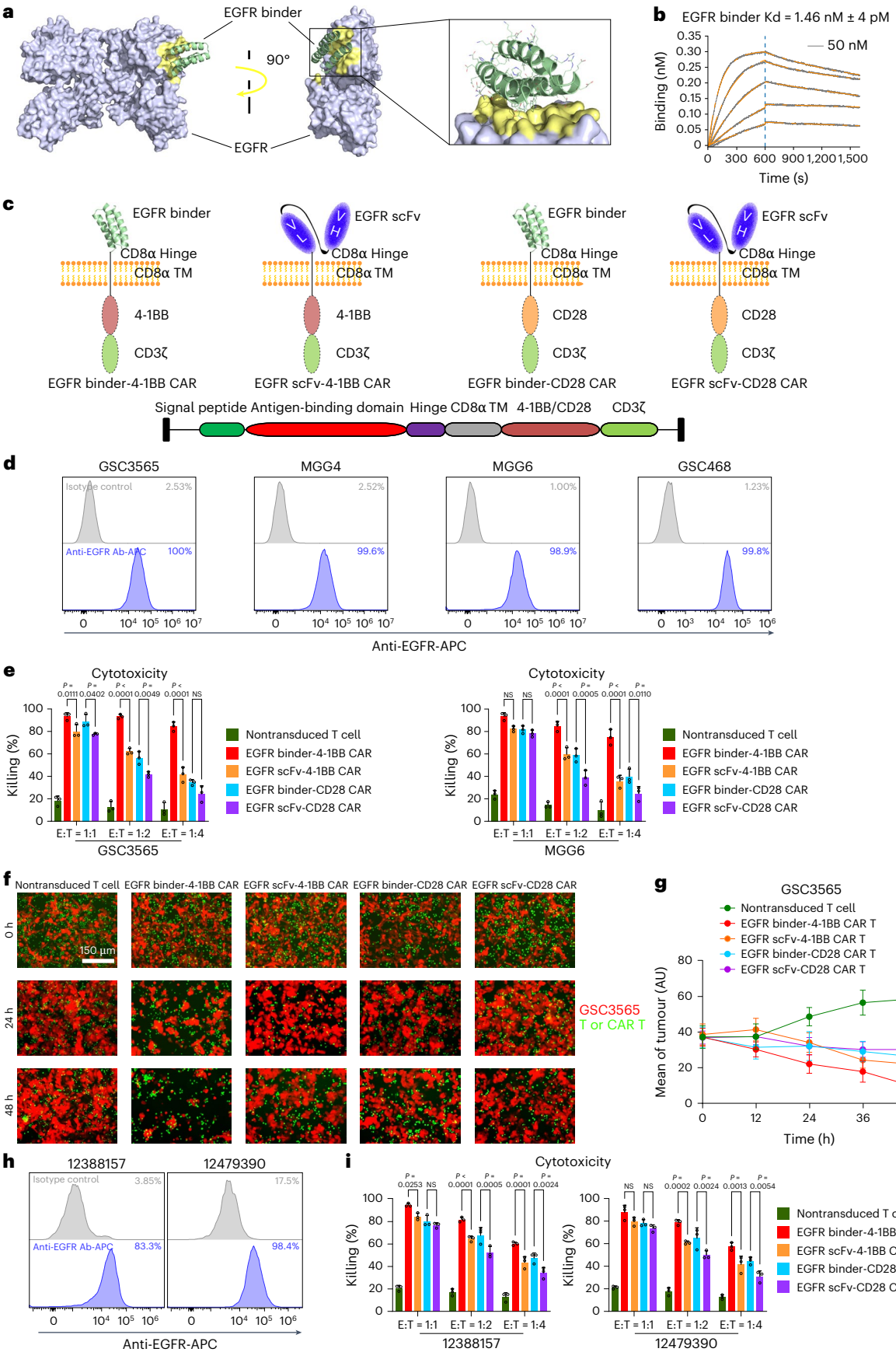

https://doi.org/10.1038/s41551-024-01258-8

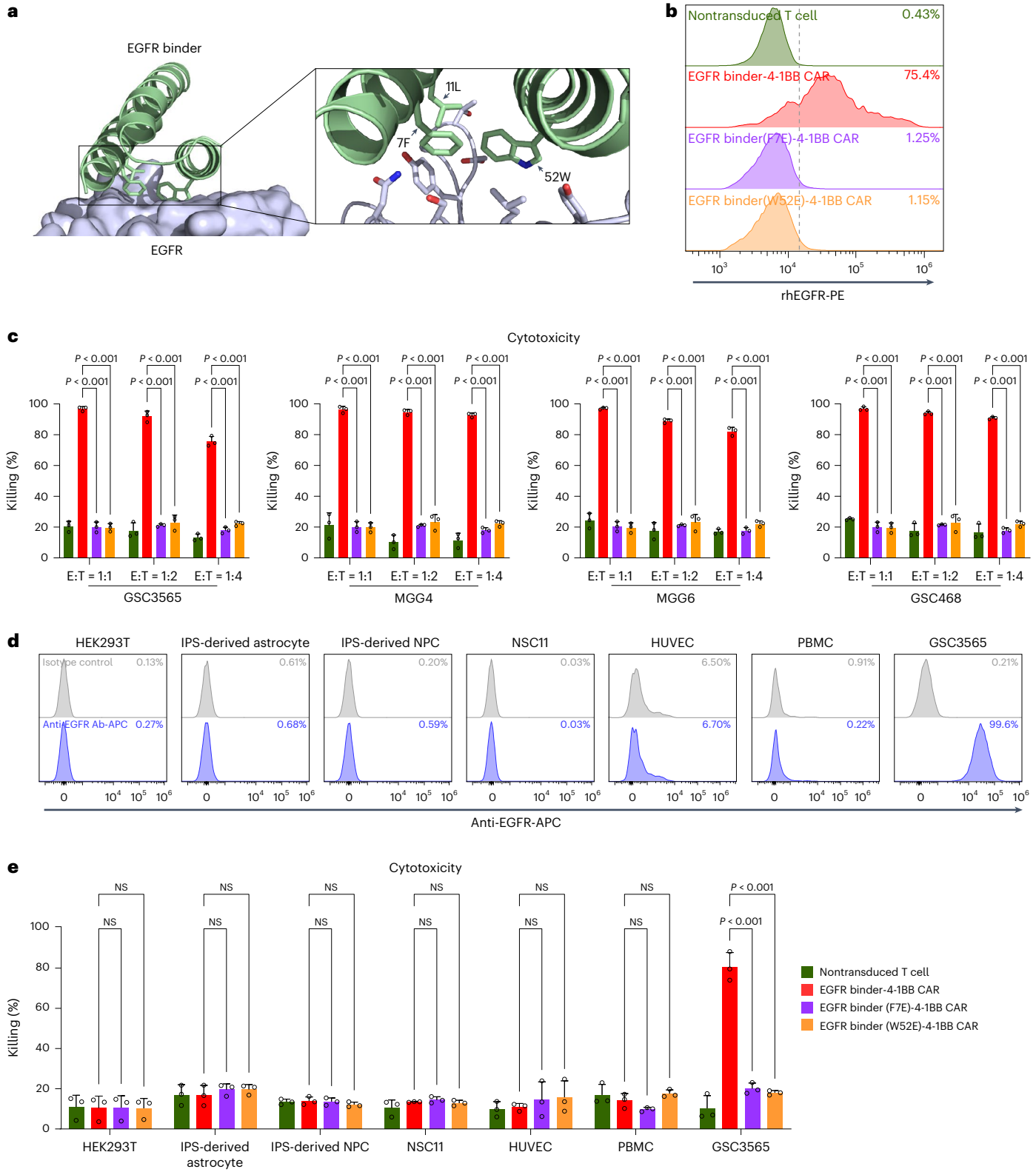

Fig. 2 | Specificity and off-target effect evaluation of EGFR binder CAR T cells. **a**, Zoomed-in view of the EGFR binder central regions. **b**, The expression of the EGFR binder and two variant (F7E and W52E) binder CARs on T cells was measured by rhEGFR protein flow cytometric staining. **c**, Percent tumour-killing activity of the indicated EGFR binder CAR T cells against cocultured GSCs at different E:T ratios. Data are shown as the mean ± s.d. (ANOVA; NS, not significant; $n = 3$). **d**, EGFR expression on non-tumoural HEK293T cells, astrocytes, NPCs, NSC11 cells, HUVECs and PBMCs was measured by anti-EGFR antibody flow cytometric staining. GSC3565 cells were used as a positive control. **e**, Percent tumour-killing activity of the indicated CAR T cells against cocultured non-tumoural HEK293T cells, astrocytes, NPCs, NSC11 cells, HUVECs and PBMCs. GSC3565 cells were used as a positive control. Data are represented as the mean ± s.d. (ANOVA; NS, not significant; $n = 3$).

https://doi.org/10.1038/s41551-024-01258-8

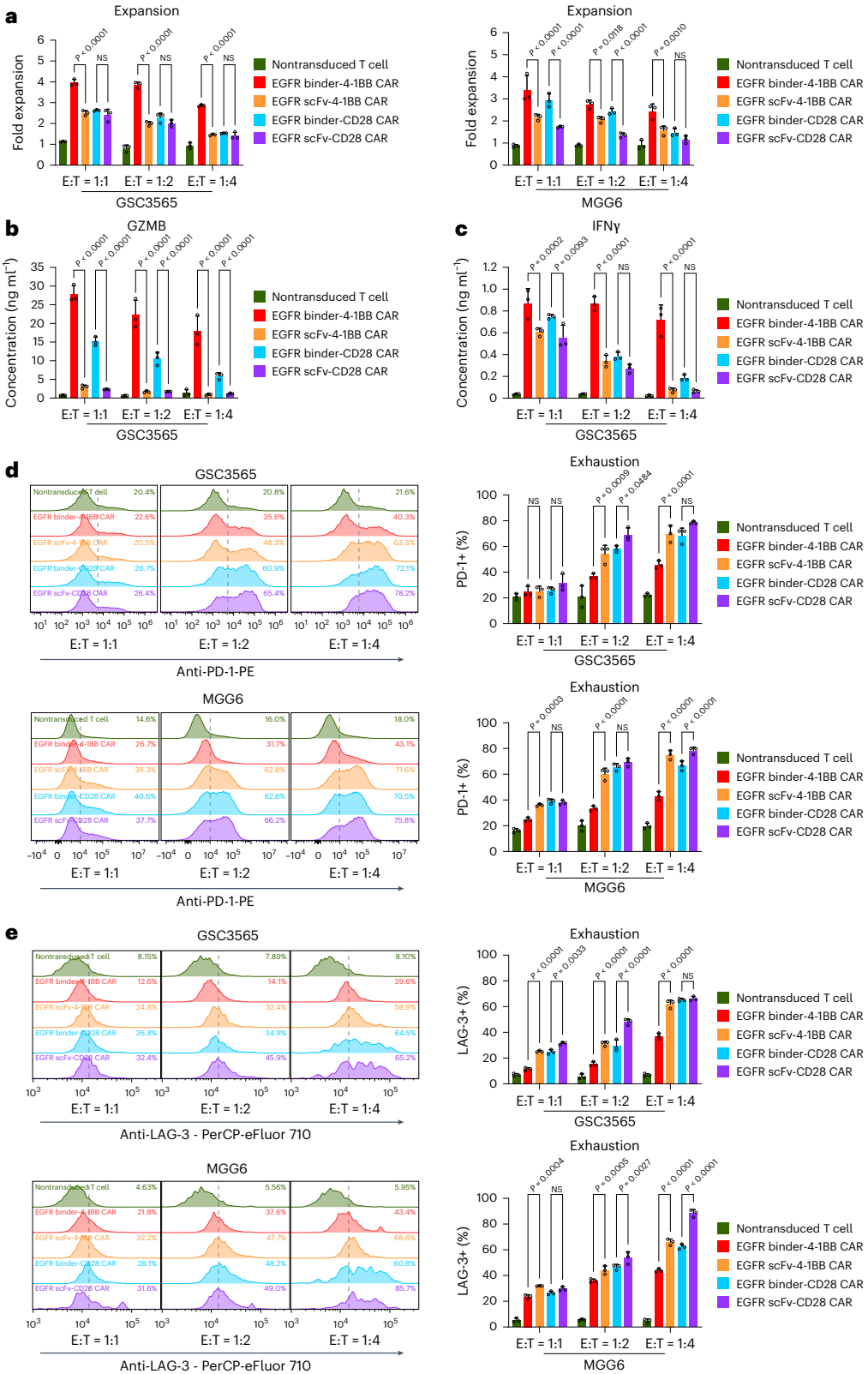

Fig. 3 | EGFR binder CAR T cells improve effector potency. a, Expansion of the indicated CAR T cells in cocultures with GSC3565 or MGG6 cells at gradient E:T ratios. Data are represented as the mean ± s.d. (ANOVA; NS, not significant; $n = 3$). **b**, GZMB secretion of the indicated CAR T cells in cocultures with GSC3565 or MGG6 cells at gradient E:T ratios. Data are represented as the mean ± s.d. (ANOVA; NS, not significant; $n = 3$). **c**, IFNγ secretion of the indicated CAR T cells in cocultures with GSC3565 cells at gradient E:T ratios. Data are represented as the mean ± s.d. (ANOVA; NS, not significant; $n = 3$). **d**, The expression of the exhaustion marker PD-1 in the indicated CAR T cells was measured after coculture with GSC3565 or MGG6 cells at gradient E:T ratios for 48 h. Data are represented as the mean ± s.d. (ANOVA; NS, not significant; $n = 3$). **e**, The expression of the exhaustion marker LAG-3 in the indicated CAR T cells was measured after coculture with GSC3565 or MGG6 cells in gradient E:T ratios (1:1, 1:2 and 1:4) for 48 h. Data are represented as the mean ± s.d. (ANOVA; NS, not significant; $n = 3$).

EGFR binder CAR T cells exhibit stronger effector potency than scFv CAR T cells

We next systematically compared the effector potency of EGFR binder CAR T cells with that of scFv CAR T cells, leveraging in vitro CAR T cell–tumour cell coculture systems. Compared with scFv CAR T cells, EGFR binder CAR T cells expanded more rapidly (Fig. 3a and Extended Data Fig. 2a,b) and secreted much greater amounts of cytotoxic factors, including granzyme B (GZMB) and interferon-γ (IFNγ) (Fig. 3b,c and Extended Data Fig. 2c–f), which was consistent with our findings shown in Fig. 1. CAR T cell exhaustion is one of the major issues limiting the efficacy of this therapy in solid tumours. Therefore, we then evaluated EGFR binder CAR T cell exhaustion by analysing the most widely used T cell exhaustion markers, PD-1 and LAG-3 (Fig. 3d,e and Extended Data Fig. 2g,h). Compared with scFv CAR T cells, binder CAR T cells showed lower expression of PD-1 and LAG-3 after tumour cell challenge, suggesting that the binder CAR T cells were more resistant to exhaustion. Furthermore, we observed that binder CAR T cells showed notably lower tonic signalling than scFv CAR T cells (Extended Data Fig. 2i–l), which has been reported as a critical factor in limiting the antitumour activity of CAR T cells[19,32,33]. Notably, CAR T cells with the 4-1BB costimulatory domain performed better than those with the CD28 costimulatory domain in terms of cytotoxic cytokine production, CAR T cell proliferation and exhaustion resistance, which was consistent with previous studies and our data shown in Fig. 1. Therefore, we decided to leverage the 4-1BB costimulatory domain in subsequent EGFR CAR T cell studies.

EGFR binder CAR T cells alter transcriptional profiles and subsets associated with effector potency

To further investigate the molecular mechanisms underlying the regulation of EGFR binder-4-1BB CAR T cell activity, we performed bulk RNA sequencing (RNA-seq) to analyse the differences in the transcriptome between binder and scFv CAR T cells. Compared with stimulated scFv CAR T cells, stimulated binder CAR T cells upregulated critical regulators of activation or cytotoxicity (GZMB and GZMA) and the cell cycle (MKI67 and CDK4) (Fig. 4a). Pathway enrichment analysis identified that cell cycle-, proinflammatory cytokine signalling- and T cell activation-related signalling pathways (activated proliferation, TCR signalling and cytotoxicity) were considerably enriched in EGFR binder CAR T cells compared with EGFR scFv CAR T cells (Fig. 4b,c and Extended Data Fig. 3a,b).

To determine the impact of different antigen-targeting domain designs (binder versus scFv) on specific subpopulations of CAR T cells, we then performed comparative single-cell RNA sequencing (scRNA-seq) on binder CAR T cells and scFv CAR T cells with or without GSC challenge. Unbiased clustering of pooled data identified 12 different subclusters, the distributions of which were changed by GSC stimulation (Fig. 4d and Extended Data Fig. 3c,d). $CD4^+$ and $CD8^+$ CAR T cells were well distinguished (Fig. 4e). Compared with scFv CAR T cells, binder CAR T cells increased the proportions of clusters 6 and 5, which highly expressed activation (GZMB, TNF, XCL1 and XCL2) or proliferation (MKI67, TOP2A, CDK1, CCNB2 and PCNA) marker genes after tumour cell stimulation, which was consistent with our bulk RNA-seq data (Fig. 4e–h and Extended Data Fig. 3e). We also found that the proportion of subcluster 8, which had high expression of inhibitory receptors (CTLA4, PDCD1, TIGIT and KLRB1), was increased in only scFv CAR T cells after tumour cell stimulation (Fig. 4e,h), further supporting our finding shown in Fig. 3d,e that binder CAR T cells are more resistant to exhaustion. Taken together, our single-cell data identified the preservation or expansion of certain CAR T cell subclusters after tumour challenge. These subclusters represented signatures of T cell proliferation, activation, cytotoxicity and exhaustion (Fig. 4h). This observation provided insight into the mechanisms underlying the superior efficacy of binder CAR T cells in targeting tumour cells.

High expression and stability of EGFR binder CAR

To further investigate the mechanisms underlying the enhancement of EGFR binder CAR T cell effectors, we assessed the CAR transduction efficiency of independent T cell lots and the expression levels of CAR molecules on the T cell membrane surface. Our binder CAR design improved transduction efficiencies of viral vector-based CARs and increased CAR expression on the T cell surface membrane (Fig. 5a,b and Extended Data Fig. 4a,b). This finding provides a possible explanation for the improvement in antitumour efficacy observed with our EGFR binder CAR T cells, particularly at low effector-to-target (E:T) ratios.

Accumulating evidence suggests that CAR downmodulation induced by tumour challenges limits CAR T cells antitumour efficacy in solid tumours[34–36]. Therefore, we quantified CAR expression levels on the CAR T cells after coculturing them with tumour cells by flow cytometry and immunoblot assays. In contrast to the EGFR scFv CAR, in which the surface CAR expression level decreased by 70%, EGFR binder CAR still maintained about 75% surface CAR expression after 48 h tumour challenging (Fig. 5c–e). To test whether similar results can be observed in vivo, we isolated tumour-infiltrating CAR T cells. Our results indicate that binder CAR T cells maintain surface CAR expression more persistently than scFv CAR T cells in vivo (Extended Data Fig. 4c), which is consistent with the phenomenon observed in vitro. To exclude the possibility that the binder CAR generates more newly synthesized CAR protein instead of resisting CAR downmodulation, we treated the CAR T cells with cycloheximide (CHX), a protein synthesis inhibitor, during the tumour challenge. The EGFR binder CAR retained about 80% of the initial surface CAR protein on the T cell membrane after 6 h of CHX treatment, while the EGFR scFv CAR only retained less than 25% of the initial surface CAR protein (Fig. 5f,g). These results suggest that the EGFR binder CAR is more resistant to tumour-induced downregulation of surface CAR expression, which is critical for maintaining the antitumour potency of CAR T cells in the solid tumour microenvironment.

Modulating the binding affinity of the EGFR binder within a certain range does not affect CAR T cell activity

The relationship between scFv binding affinity and CAR T cell activity was controversial, as reported by previous studies[37,38]. Compared with the traditional scFv CAR, our DNDB made it easy to precisely manipulate

Fig. 4 | EGFR binder CAR T cells alter transcriptional profiles associated with effector potency. a, Gene expression differences in RNA-seq data between EGFR binder and EGFR scFv after GSC3565 cell stimulation. Genes with $\log_2$(fold change) > 1 and false discovery rate (FDR) < 0.05 are marked in red. Genes with $\log_2$(fold change) < −1 and FDR < 0.05 are marked in blue. Other genes are marked in grey. **b**, Signalling pathways enriched in EGFR binder-4-1BB CAR T cells compared with EGFR scFv-4-1BB CAR T cells after stimulation with GSC3565 cells. **c**, GSVA enrichment scores for gene sets including cell proliferation- and cytotoxicity-related genes before and after stimulation. **d**, UMAP plot of single-cell RNA-seq data for EGFR binder-4-1BB CAR T cells and EGFR scFv-4-1BB CAR T cells both before and after stimulation with GSC3565 cells. Cluster composition of unstimulated versus stimulated EGFR-binder or EGFR-scFv cell populations. **e**, Characterization of clusters with functional T cell markers. Top, violin plot of MKI67 expression. Middle, dot plot of CD4 versus CD8A expression; larger dots indicate a higher proportion of cells with expression, and red versus blue indicates higher expression. Heatmap, scaled expression of T cell markers including markers for naive cells, cell proliferation, AP-1 signalling, cytokines, activation, inhibitory markers and exhaustion-related transcription factors. Bottom, the proportion of cells in each cluster under stimulated versus unstimulated conditions in EGFR binder-4-1BB CAR T cell populations (red) or EGFR scFv-4-1BB CAR T cell populations (blue). Positive values indicate an increase in cluster occupancy following GSC3565 cell stimulation. **f**,**g**, Expression of GZMB (**f**) and MKI67 (**g**) in unstimulated versus stimulated EGFR binder-4-1BB or EGFR scFv-4-1BB CAR T cell populations. **h**, Distribution of functional status scores in selected clusters.

https://doi.org/10.1038/s41551-024-01258-8

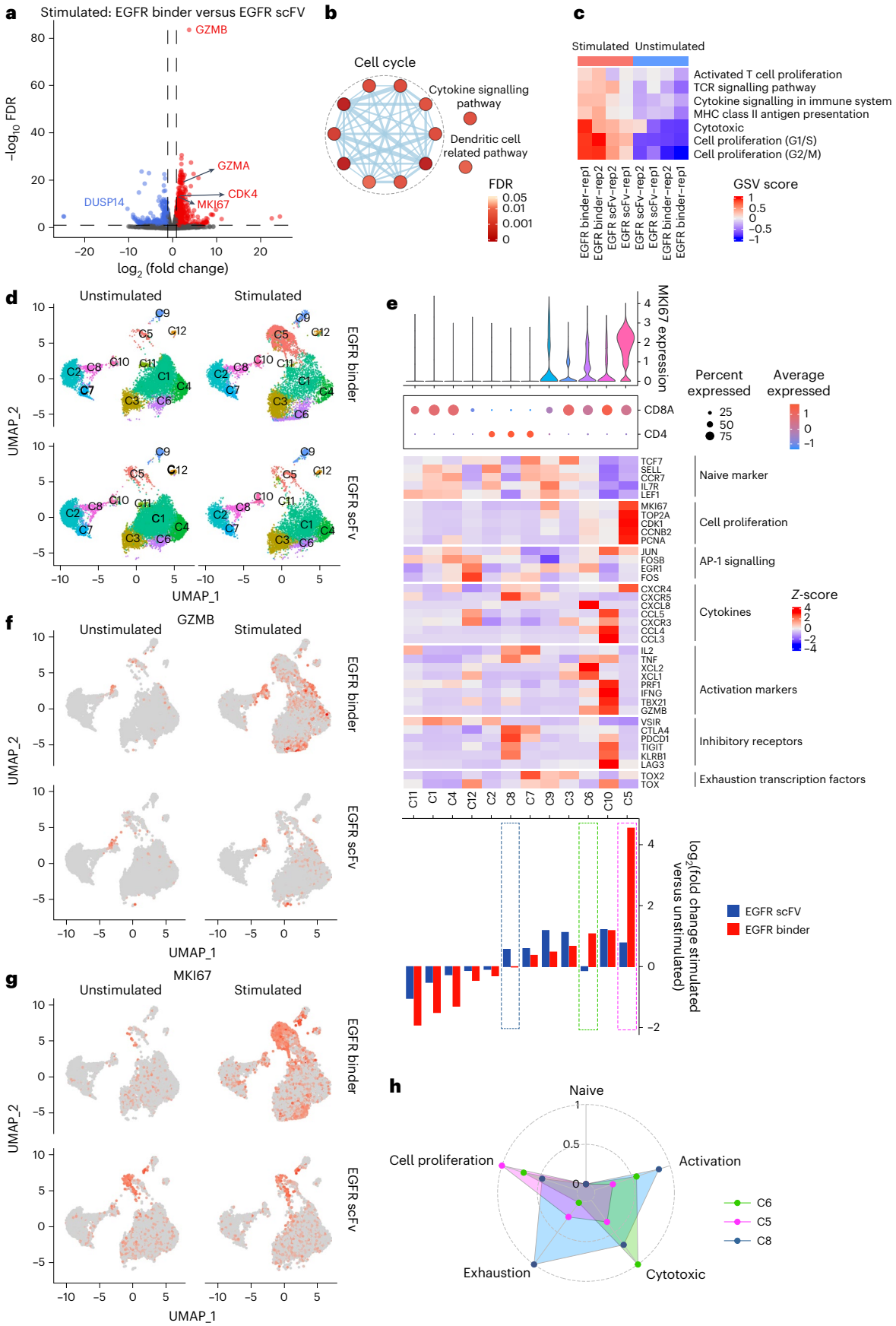

the binding affinity for the target protein without changing the binding epitope. Therefore, we generated a set of EGFR binder variants by mutating some key large hydrophobic residues to smaller ones at the binding interface, which resulted in a wide range of changes (kD 55 nM to 1,200 nM) in the binding affinity for EGFR (Fig. 2a and Extended Data Fig. 5a–e). We further evaluated the effector functions of these binder variant CAR T cells. Interestingly, we found that changing the binding affinity of the binder over a wide range (kD 1.46 nM to 180 nM) did not affect CAR T cells tumour killing, proliferation or exhaustion in a single round of tumour challenge. However, only CARs with high-affinity binders (kD 1.46 nM to 55 nM) maintained a strong tumour-killing efficiency and cell viability, and demonstrated relatively low exhaustion after multiple rounds of challenge. By contrast, CARs with low-affinity binders (kD 130 nM to 1,200 nM) did not exhibit these characteristics throughout multiple rounds of challenge (Extended Data Fig. 5f–h). Our results suggest that binder CAR T cells have the potential advantage of convenient adjustment of their affinity.

EGFR binder CAR T cells exhibited enhanced antitumour activity in vivo

To evaluate the antitumour activity of EGFR binder CAR T cells in vivo, we leveraged orthotopic glioblastoma xenograft models established by intracranial transplantation of two different GSC lines (MGG6 and GSC3565). Ten days after transplantation, GSC-bearing mice were treated with binder CAR T cells, scFv CAR T cells or nontransduced control T cells (Fig. 6a). Compared with scFv CAR T cell treatment, both binder CAR T cell treatments inhibited tumour growth and prolonged mouse survival (Fig. 6b–d and Extended Data Fig. 6a–c), which was consistent with their antitumour activity in vitro. We also found that EGFR binder CAR T cell treatment did not reduce mouse body weight, indicating the low toxicity of this therapy (Fig. 6e and Extended Data Fig. 6d). The analysis of tumour-infiltrating CAR T cells reveals that binder CAR T cells exhibit a higher abundance and lower exhaustion level in mice over time (Fig. 6f,g). This finding suggests that binder CAR T cells show prolonged persistence and increased resistance to exhaustion compared with scFv CAR T cells. To further evaluate the efficacy of binder CAR T cells, we conducted additional experiments by incorporating both binder and scFv CAR into mouse T cells, and by overexpressing human EGFR (hEGFR) in mouse glioma cell GL261 as the target antigen (Extended Data Fig. 7e–g). Compared with scFv CAR T cell treatments, both binder CAR T cell treatments also prolonged immunocompetent mouse survival without a detectable toxicity (Fig. 6h–j). In addition, we injected healthy C57BL/6 mice with the same dosage of CAR T cells to assess safety. Following intracerebral injection of mouse CAR T cells, we observed no body weight loss or morphological alterations in multiple organs, including the brain, colon, heart, intestine, kidney, liver, lung and spleen (Extended Data Fig. 7h,i). Our results indicated that binder CAR T treatment effectively prolonged the survival time of tumour-bearing mice to a greater extent than scFv CAR T treatment, without causing any discernible toxic side effects in immunocompetent mice. In summary, EGFR binder CAR T cells showed enhanced antitumour properties and limited toxicity in orthotopic glioblastoma xenograft models.

CD276 binder CAR T cells efficiently target CD276-expressing glioblastoma cells

To test whether the binder-based CAR approach can be further applied to targets other than EGFR, we selected CD276 (B7-H3), a promising tumour-associated antigen in multiple ongoing CAR T cell clinical trials for many different solid tumours, including glioblastoma[39], as a second target for binder CAR design. Utilizing our previously described computational protein binder design strategy[27], we designed mini-protein binders targeting the N-terminal IgV domain of CD276 (Fig. 7a). DNA oligos encoding the designed binders were synthesized as a pool and displayed on the surface of yeast for high-throughput screening. After several rounds of screening using fluorescently labelled CD276 protein, we identified a promising CD276 binder candidate, CD276 mb (Fig. 7b), which could bind with CD276 with low nanomolar affinity (Fig. 7d). We then generated the site-saturation mutagenesis (SSM) library of CD276 mb, in which every residue was substituted with each of the 20 amino acids one at a time, and screened the library with more stringent screening conditions by lowering down the target concentration. We identified one variant with mutation L32V via Sanger sequencing of the yeast clones from the final sorted library. This mutant showed roughly twofold increase compared with the parent design (Fig. 7e). Further analysis of each sorted pool of the SSM library by deep sequencing showed that the substitutions at the designed binding interface and in the protein core of CD276 mb were less tolerated than substitutions at non-interface surface positions (Fig. 7c), suggesting that the folding of CD276 mb and binding configuration are correct. By combining the beneficial mutations identified from the SSM analysis and screening the combinatorial library, we obtained the final affinity-matured binder HM9 with little or no immune response in vivo, which could bind to CD276 with low picomolar affinity in the biolayer interferometry (BLI) assay (Fig. 7f and Extended Data Fig. 7a). We then designed CD276 CAR based on the computationally designed CD276 mb and its optimized variants to test the general applicability of our CAR T design strategy. We also used a CD276-specific scFv (clone 376.96) CAR, which has shown strong antitumour activity in previous studies[40,41], as a positive control. Both CD276 binder and scFv can bind to the actual tumour-associated antigens (Extended Data Fig. 7b). We next evaluated the effector potencies of these CAR T cells coculturing them with two GSC lines (GSC3565 and MGG6) with high expression of CD276 (Fig. 7g). CD276 binder CAR T cells showed greater tumour killing and exhaustion resistance at low E:T ratios (1:4 and 1:16) than scFv CAR T cells, while only HM9 CAR T showed a stronger ability in cell proliferation (Fig. 7h–j and Extended Data Fig. 7c–f). CD276 mb_L32V and HM9 CAR T cells also showed a greater cytotoxic cytokine secretion than scFv CAR T cells (Fig. 7k,l and Extended Data Fig. 7g,h). The transduction efficiencies of viral vector-based CARs, as well as the expression levels of CAR, were notably improved in HM9 CAR T cells compared with CD276 scFv CAR T cells (Extended Data Fig. 7i,j). Encouragingly, CD276 HM9 CAR T cell

Fig. 5 | Design of EGFR binder CAR enhances CAR transduction, surface expression and stability. a, The percentage of CAR transduction is shown for paired samples of EGFR binder and EGFR scFv 4-1BB CAR T cells with a gradient dose of lentivirus (*t*-test; $n = 7$). **b**, CAR surface expression (localization number/area (N/μm^2)) is counted by STORM imaging. Blue dashed lines indicate the cell membrane boundaries drawn manually. Pseudocolour is used to show the local expression density of CAR molecule. STORM imaging was performed on a custom-built super-resolution microscope using an oil objective (100× 1.5 NA, UPLAPO100XOHR, Olympus), and it is analysed by ImageJ software. The boxes depicted the upper and lower quartiles of the data, while the whiskers represented the entire range of points, from the minimum to the maximum values (paired *t*-test; $n = 7$). **c**, Surface CAR expression level was measured by flow cytometry. EGFR binder CAR T cells (left) or EGFR scFv CAR T cells (right) were cocultured with or without GSC3565 for 48 h. Mean fluorescence intensity was obtained to calculate the percentage of surface CAR degradation in EGFR binder and EGFR scFv CAR T cells (paired *t*-test; $n = 3$). **d**, Representative immunoblot analysis of surface CAR expression level on EGFR binder CAR T cells and EGFR scFv CAR T cells membrane during challenging with GSC3565 cells. **e**, Quantification of surface CAR expression levels on EGFR binder CAR T cells and EGFR scFv CAR T cells membranes normalized to ATP1A1 levels ($n = 3$) during challenging with GSC3565 cells. **f**, Representative immunoblot analysis of surface CAR expression levels on EGFR binder CAR T cells and EGFR scFv CAR T cells membranes during challenging with GSC3565 cells in the presence of 10 μg ml^{-1} CHX. **g**, Quantification of surface CAR expression levels on EGFR binder CAR T cells and EGFR scFv CAR T cells membranes normalized to ATP1A1 levels ($n = 3$) during challenging with GSC3565 cells in the presence of 10 μg ml^{-1} CHX.

https://doi.org/10.1038/s41551-024-01258-8

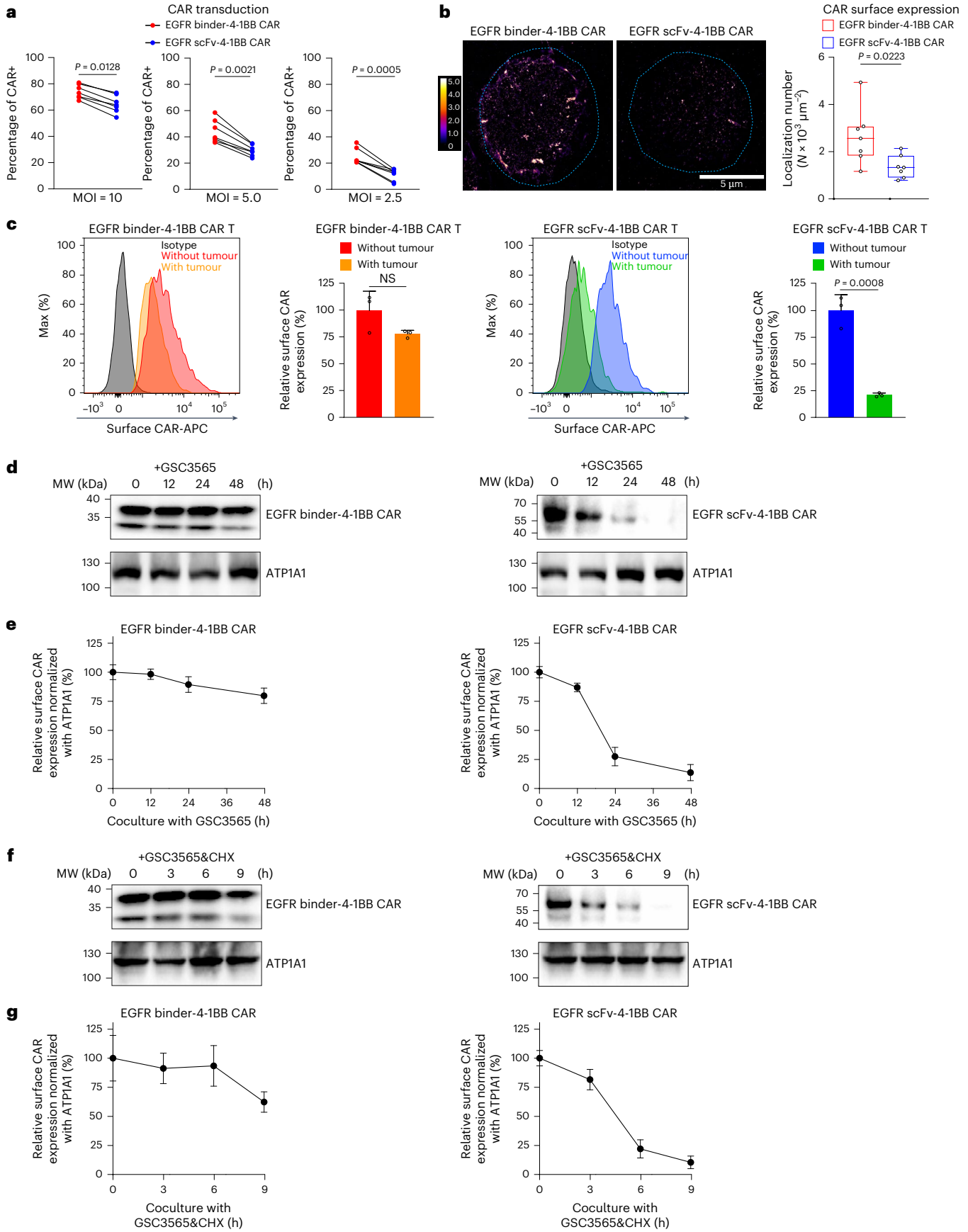

https://doi.org/10.1038/s41551-024-01258-8

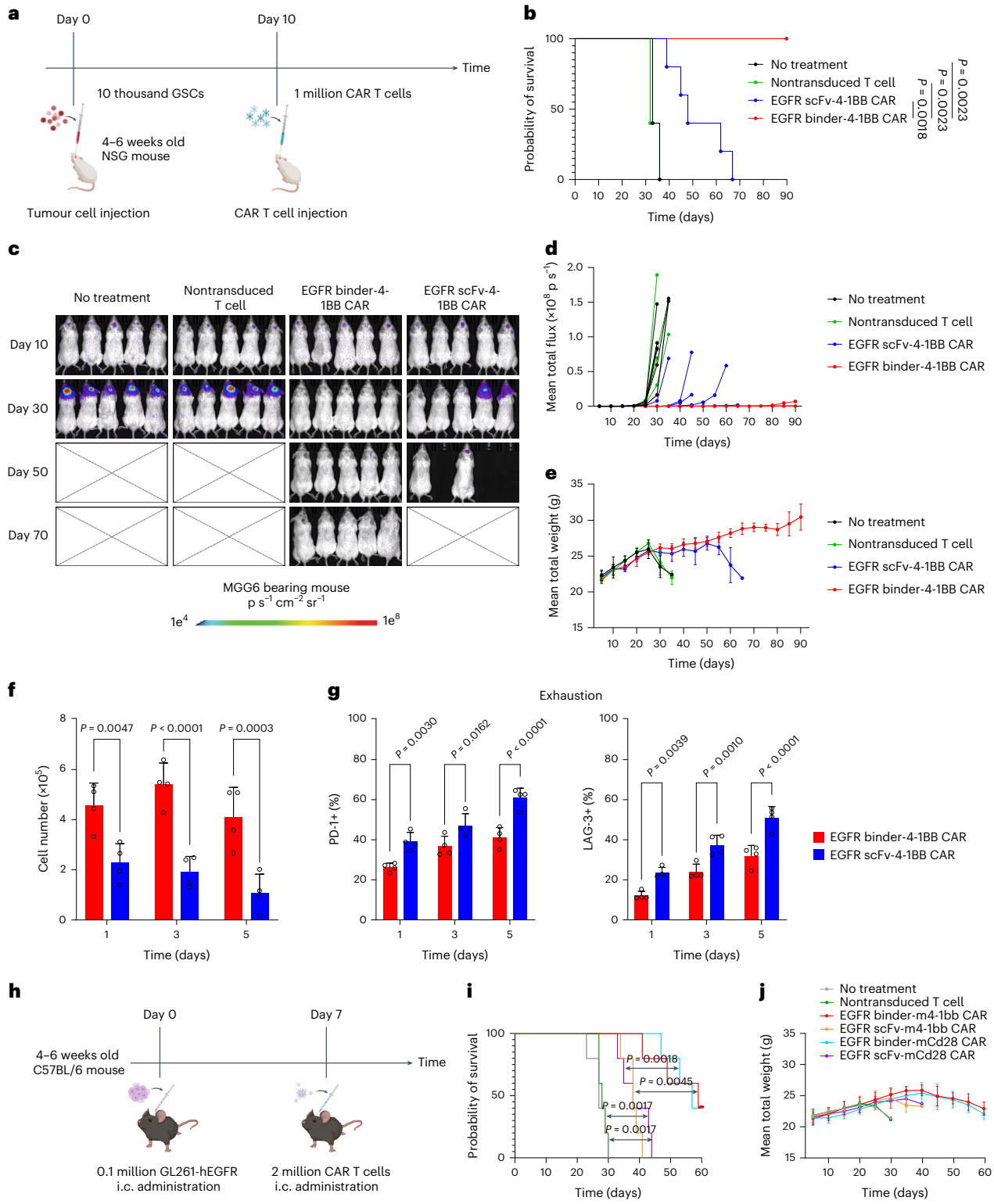

Fig. 6 | EGFR binder CAR T cells exhibited enhanced antitumour activity in vivo. a, Schematic of the in vivo orthotopic CAR T cell therapy for a glioblastoma-bearing mouse model. Tumours were established by orthotopically implanting 10,000 GSCs and then treated with 1 million CAR T cells in situ 10 days after tumour cell injection. Created with BioRender.com. **b**, Kaplan–Meier survival curves of mice bearing intracranial MGG6 cells treated with control T cells, EGFR binder-4-1BB CAR T cells or EGFR scFv-4-1BB CAR T cells. *P* values were calculated using the log-rank test ($n = 5$). **c**,**d**, Bioluminescence imaging to measure MGG6 tumour cell growth in vivo. **e**, Body weight measurement of mice in the indicated treatment groups. **f**,**g**, Collect and digest tumour tissues at 1, 3 and 5 days after CAR T therapies, and the tumour-infiltrating CAR T cells were isolated and quantified (**f**). The expression of the exhaustion markers PD-1 and LAG-3 in the indicated CAR T cells was measured by flow cytometry (**g**). Data are represented as the mean ± s.d. (ANOVA; $n = 4$). **h**, Scheme of experimental details. Tumours were established by orthotopically implanting 0.1 million GL261-hEGFR and then treated with 2 million mouse CAR T cells in situ 7 days after tumour cell injection. Created with BioRender.com. **i**, Kaplan–Meier survival curves of mice bearing intracranial GL261-hEGFR cells treated with control T cells, EGFR binder-m4-1bb/-mCd28 CAR T cells or EGFR scFv-m4-1bb/-mCd28 CAR T cells. *P* values were calculated using the log-rank test ($n = 5$). **j**, Body weight measurement of mice in the indicated treatment groups. i.c., intracranial.

https://doi.org/10.1038/s41551-024-01258-8

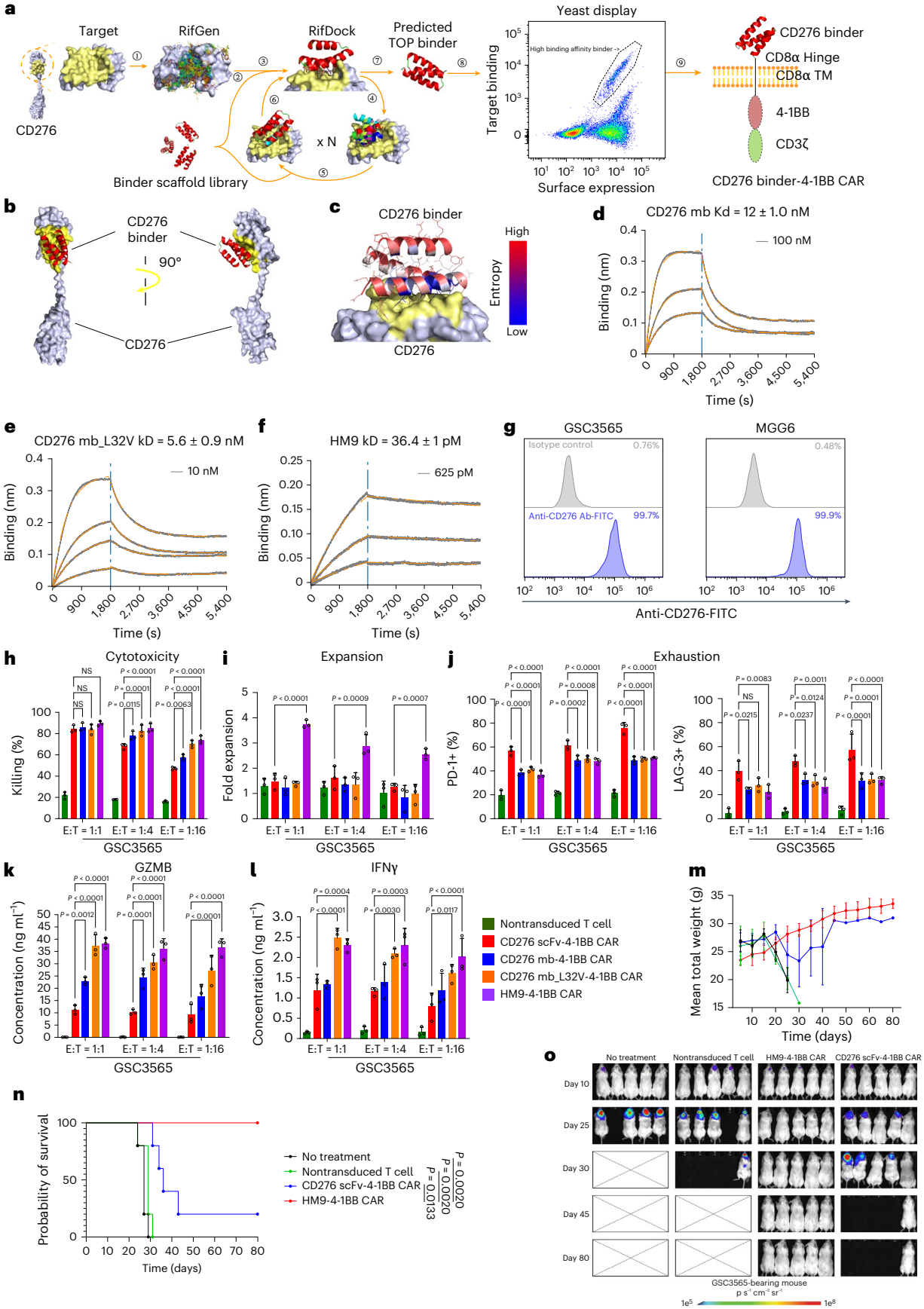

Fig. 7 | CD276 binders improve CAR T cell antitumour potency. a, Schematic of the CD276 binder design pipeline. Step I: generate billions of docked rotamers around the target binding region. Step II: dock three-helix bundle scaffolds on the target. Step III: design sequence with Rosetta FastDesign. Step IV: extract and screen great motifs. Step V: graft motifs on scaffolds. Step VI: design sequence with Rosetta FastDesign. Step VII: predict binder structure with AlphaFold2, and screen top 10,000 binders based on AlphaFold2 scores and Rosetta scores. Step VIII: order a DNA library containing all binder sequences, and screen with a yeast display. Step IX: sequence the yeast clone containing the highest binding affinity binder, extract the sequence, and integrate it into the CAR structure. **b**, Predicted CD276 binder complex structure. The PDB identifier was 4I0K (CD276). **c**, CD276 binder complex structure is coloured by positional Shannon entropy, low entropy positions (conserved, blue) and high entropy positions (not conserved, red). **d**–**f**, Biolayer interferometry characterization of the binding of the CD276 mb (**d**), CD276 mb_L32V (**e**) and HM9 (**f**) to CD276. **g**, The CD276 expression on different GSC lines (GSC3565 and MGG6) was measured by anti-CD276 antibody flow cytometric staining. **h**–**l**, Cytotoxicity (**h**), expansion (**i**), exhaustion (**j**), GZMB secretion (**k**) and IFNγ secretion (**l**) evaluations of the indicated CAR T cells in cocultures with GSC3565 at gradient E:T ratios. Data are shown as the mean ± s.d. (ANOVA; NS, not significant; $n = 3$). **m**, Body weight measurement of mice in the indicated treatment groups. **n**, Kaplan–Meier survival curves of mice bearing intracranial GSC3565 cells treated with control T cells, HM9-4-1BB CAR T cells or CD276 scFv-4-1BB CAR T cells. *P* values are calculated using the log-rank test ($n = 5$). **o**, Bioluminescence imaging to measure GSC3565 tumour cell growth in vivo.

treatments resulted in suppressed tumour growth, prolonged mouse survival and no notable toxic side effects compared with the CD276 scFv CAR T group (Fig. 7m–o and Extended Data Fig. 7k). Taken together, our findings suggest that binder-based CAR T cell designs can be extensively utilized against various targets, potentially providing clinical benefits.

Discussion

Despite notorious success against haematological malignancies, CAR T cell therapy remains challenging in solid tumours[42]. To overcome this, vast efforts have been made to improve CAR design, and most have focused on the intracellular signalling domains of the CAR structure. In this study, we developed a strategy leveraging a DNDB instead of a typical scFv as the tumour surface antigen-binding domain to enhance CAR T cell antitumour potency.

Computational protein design has advanced to a point where it is possible to generate de novo protein binding proteins just using the target structure information, with high binding affinities and precisely tailored binding configurations to perform the desired functions[27]. The binders have been increasingly applied to address real-world challenges in biomedicine and biological engineering. We recently designed picomolar SARS-CoV-2 virus inhibitors, which showed strong neutralization for most circulating SARS-CoV-2 variants in animal-level studies[26]. Another example showed that the de novo-designed interleukin-2 (IL-2) mimetic Neoleukin-2/15 (Neo-2/15) induces potent immunotherapeutic effects with reduced toxicity when compared with natural IL-2[25], and its split, conditionally active version could further reduce the toxicity of systemic cytokine therapy[43]. Our results further showcase the substantial potential of DNDBs in the development of immunotherapy. For this study, we selected human EGFR and human CD276 as target antigens for CAR T immunotherapy, but the computational binder design pipeline and CAR design strategy can in principle be applied to any clinically validated targets highly expressed on the tumour cell surface. Our results not only open the door to a class of CAR T design strategies but also applications of DNDBs in the development of more effective immunotherapy in tumour treatment.

Owing to their high engineerability, we generated a set of binder variants via single-site mutagenesis based on the design model of the EGFR binder. The binder variants showed different binding affinities over a range; however, the CAR T cell tumour-killing efficiency, proliferation or exhaustion remained the same. Our results are in agreement with previous findings[44–46], which suggest that binding affinity of CAR is not a key determinant of developing effective CAR T therapy. However, the final affinity-matured CD276 binder showed greater killing capability compared with the initial designed binder and the affinity-improved single-mutation variant. More experimental data collected over different binders and over different targets are needed to further illustrate the relationship between binding affinity and CAR T therapy efficacy. Moreover, DNDBs targeting different regions of the same target can be generated and comparing their relative effectiveness in the CAR T system is also an attractive research area. This will not only lead to the development of more effective CAR T therapies but also offers tools and opportunities for investigating the underlying mechanism of T cell activation, proliferation and exhaustion.

The superior antitumour performance of our DNDB-CAR T lies in the binder's remarkable biochemical and biophysical properties that (often) exceed those of natural protein-derived binding agents, such as scFvs. The DNDBs are designed based on the basic principles of protein folding and binding, and mainly consist of regular secondary structures and short loops. Thus, the DNDBs can usually be expressed with high yield in recombinant systems, and they are extremely thermostable, highly soluble in solution and well tolerate to mutations and modifications. Conversely, scFv often suffers from aggregation, solubility and stability issues, which limits its manufacturability and clinical development[23]. It has been reported that tumour antigens trigger CAR degradation, leading to dysfunction of CAR T cells. In this study, we demonstrated that binder-based CARs are more stable and resistant to tumour antigen-induced downregulation[35]. This characteristic holds implications for CAR T cell functionality within the solid tumour microenvironment, where CAR T cells are surrounded by a multitude of tumour cells. Moreover, our DNDB consisted of only approximately 60 amino acids, which is much smaller than antibody-based scFvs (approximately 230 to 250 amino acids) and nanobodies (approximately 110 to 130 amino acids)[47]. Using a binder reduces the total size of the whole CAR construct, thus improving the packaging and transduction efficiencies of viral vector-based CARs or enhancing the genome integration efficiency of nonviral vector-based CARs. Some studies have shown encouraging progress in overcoming the heterogeneity of haematological malignancies using dual-targeted CAR T cells targeting two different tumour-associated antigens. Our mini-sized binders make it possible to design CAR T cells that target multiple tumour antigens within one construct for use against more heterogeneous solid tumours. Interestingly, a recent study proposed a size-dependent activation model for CAR T cells and showed that CAR T cell activation decreased with increasing length of the CAR extracellular domain[48]. This finding is consistent with our binder CAR T cell activation data and supports the superiority of designing a small CAR antigen-binding domain.

A growing body of evidence indicates that CARs often undergo rapid downmodulation after engaging with tumour antigens[34,36,49–51]. Such downmodulation could potentially attenuate the tumour-killing ability of CAR T cells following prolonged engagement with tumour antigens[36]. Further, it has been reported that tumour antigen-induced CAR downmodulation can limit the antitumour efficacy within the tumour microenvironment in solid tumour models[34]. Interestingly, blocking this CAR downmodulation can enhance CAR T cell functions and lead to superior persistence in vivo[35]. These findings imply that maintaining CAR surface expression may be key to promoting CAR T efficacy. In this context, our observation is that binder CAR is more resistant to tumour-induced downregulation of surface CAR expression, as it suggests a potential for maintaining the antitumour potency of CAR T cells in the solid tumour microenvironment.

Our EGFR and CD276 binder CAR T cells are not only limited to targeting glioblastoma but may also be effective in treating

many other types of solid tumours that highly express EGFR or CD276, such as non-small-cell lung cancer and pancreatic ductal adenocarcinoma[52–55]. Furthermore, exploring the impact of DNDBs for other tumour-associated antigens on the antitumour efficacy of CAR T cell therapies in future studies would be of great interest.

Methods

Cell models

HEK293T cells were purchased from American Type Culture Collection (CRL-3216, ATCC) and cultured in DMEM (#C11995500CP, Gibco) supplemented with 10% fetal bovine serum (FBS; #10099-141C, Gibco), 1% penicillin/streptomycin (SV30010, HyClone) and 1% GlutaMax Supplement (35050-061, Gibco). The cell lines GSC3565, GSC468 and GL261 were generated in our laboratory. The cell lines MGG4 and MGG6 were a kind gift from H. Wakimoto provided with a material transfer agreement from Massachusetts General Hospital. Glioblastoma primary cells were obtained from excess surgical resection samples from patients at The Second Affiliated Hospital Zhejiang University School of Medicine with appropriate consent and in accordance with an institutional review board (IRB)-approved protocol (no. IR2022453). GSCs and glioblastoma primary cells were cultured in Neurobasal-A Medium (12349-015, Gibco) supplemented with 1% B-27 supplement (12587-010, Gibco), 20 ng ml^{-1} recombinant human EGF protein (236-EG, R&D), 20 ng ml^{-1} recombinant human FGF basic protein (4114-TC, R&D), 1% penicillin/streptomycin (P/S, SV30010, Invitrogen), 1% sodium pyruvate (11360-070, Gibco) and 1% GlutaMax Supplement (35050-061, Gibco). The cell line NSC11 is a human neural stem cell line that was purchased from Alstem (hNSC11, Alstem). The HUVEC was purchased from ZQXZBIO (DFSC-EC-01, ZQXZBIO) and cultured in relevant culture medium (ZQ-1304, ZQXZBIO). Astrocytes and neural progenitor cells (NPCs) were differentiated from healthy donor-derived iPSCs following previously published protocols[56]. NSC11 cells and NPCs were cultured in the same medium as GSCs. Astrocytes were cultured in astrocyte medium (1801, ScienCell). GL261 was cultured in DMEM supplemented with 10% FBS, 1% penicillin/streptomycin and 1% GlutaMax Supplement.

Source of primary human T cells

PBMCs from healthy donors were purchased from Sailybio (China). Primary human T cell isolations followed the procedures described in the EasySep Human T Cell Isolation Kit protocol (17951, STEMCELL).

Source of primary mouse T cells

Primary mouse T cell isolations followed the procedures described in the EasySep Mouse T Cell Isolation Kit protocol (19851, STEMCELL) from mouse spleen.

DNA constructs

All human CAR constructs contained an hCD8α signalling peptide, an antigen-binding domain (scFv or protein binder), an hCD8α hinge domain, an hCD8α transmembrane domain (TM), an intracellular costimulatory domain (h4-1BB or hCD28) and an hCD3ζ intracellular signalling domain. The human CAR fragments were constructed into the pCDH-CMV-MCS-EF1-copGFP lentiviral vector (CD511B-1, System Biosciences) as lentiviral CAR vectors. Mouse 4-1BB CAR constructs contained an mCD8α signalling peptide, an antigen-binding domain (scFv or protein binder), an mCD8α hinge domain, an mCD8α TM, an intracellular costimulatory domain (m4-1bb) and an mCd3ζ intracellular signalling domain. Mouse CD28 CAR constructs contained an mCD8α signalling peptide, an antigen-binding domain (scFv or protein binder), an mCd28 hinge domain, an mCd28 TM, an intracellular costimulatory domain (mCd28) and an mCd3ζ intracellular signalling domain. The mouse CAR fragments were constructed into the MSCV-myc-CAR-2A-Thy1.1 retroviral vector (#127890, Addgene) as lentiviral CAR vectors. The EGFR scFv sequence was from NCBI (GenBank ID JQ306330.1)[30,57]; the CD276 scFv sequence was derived from the 376.96 antibody[40,41]. The binder sequences are listed as follows: EGFR binder, DHWEEVFRWALEHLQEATQQNDPQKAKKILEEAHKWLRRELSEEEARAVVRWLKQLVDRELS[27]; CD276 binder, DEERELRILERTAKALIRLNDRRLLKVLLESLEYFLRKTGDPRARELFERIKRFLD; HM9, DEEWEFRILERTAKALIRQNDRRMLKVLLESVEYFLRKTGDPRARELFERIKRFLD.

Lentivirus packaging

One 15 cm dish of HEK293T cells was co-transfected with 18 μg of lentiviral expression vector, 12 μg of packaging plasmid psPAX2 (12260, Addgene) and 6 μg of envelope plasmid pMD2.G (12259, Addgene) using polyethylenimine transfection reagent (23966-1, Polysciences). The supernatant of a HEK293T cell culture was collected twice, at 48 h and 60 h after transfection. The lentiviral product was concentrated by ultracentrifugation (XPN-100, Beckman) at 25,000 rpm for 2 h. The lentivirus was stored at −80 °C before use.

Retrovirus packaging

One 15 cm dish of Plat-E cells was transfected with 18 μg of retroviral expression vector using TransIT-293 Transfection Reagent (MIR2700, Mirus). The supernatant of a Plat-E culture was collected at 48 h after transfection. The retrovirus was freshly prepared before use.

Human CAR T cell production

To generate human CAR T cells, primary human T cells isolated from PBMCs were stimulated with Human T-Activator CD3/CD28 Dynabeads (11131D, Invitrogen) for 1 day and then transduced with a CAR-carrying lentivirus. Five days after CAR transduction, the CD3/CD28 Dynabeads were removed, and the CAR T cells were cultured in X-VIVO 15 medium (04-418Q, Lonza) supplemented with 10% FBS and recombinant human IL-2 (rhIL-2, 50 U ml^{-1}, 200-02-50, PeproTech) for further experiments. Transduction efficiency was evaluated by copGFP.

Mouse CAR T cell production

Before mouse T cell activation, 12-well plates were precoated with 1 ml of anti-mCd3 (10 μg ml^{-1}, BE0002-5MG, Bioxcell) per well at 4 °C overnight. To generate mouse CAR T cells, primary mouse T cells isolated from spleen were seeded in anti-mCd3 precoated well in mouse T cell complete culture medium (RPMI 1640 Medium (C22400500CP, Gibco) supplemented with 10% FBS, 100 U ml^{-1} rhIL-2, 1× non-essential amino acids (11140050, Gibco), 1× sodium pyruvate and 1× 2-mercaptoethanol (PB180633, Gibco)) supplemented with anti-mCd28 (10 μg ml^{-1}, BE0015-1-5MG, Bioxcell) and stimulated for 24 h.

Retrovirus mixed with active mouse T cells were added into a RetroNectin-precoated well, and spin infection at 1,500 × *g* for 90 min at 32 °C. Cells were passaged 1:2 every day with fresh complete medium. Transduction efficiency was evaluated by Thy1.1 using an anti-Thy1.1 antibody (OX-7, BioLegend).

Flow cytometry and in vitro cytotoxicity assays

For the in vitro cytotoxicity assay, CAR T cells were cocultured with GSCs at different E:T ratios. After 48 h, the numbers of remaining CAR T cells and GSCs were evaluated by flow cytometry. CAR expression was determined by staining for the recombinant human EGFR protein (EGR-HP2E3, ACROBiosystems). The antibodies used for flow cytometry were as follows: anti-hCD3 (OKT3, BioLegend), anti-PD-1 antibody (EH12.2H7, BioLegend), anti-hLAG-3 antibody (46-2239-42, Thermo), anti-hEGFR antibody (AY13, BioLegend), anti-hCD276 antibody (1188-MM06-F, SinoBio), anti-Myc-tag antibody (9B11, Cell Signaling Technology), anti-mCd3 antibody (145-2C11, BioLegend) and anti-Thy1.1 antibody (OX-7, BioLegend). All flow cytometry experiments were performed using a CytoFLEX LX (Beckman Coulter) and analysed with FlowJo X. GZMB and IFNγ secretion were quantified with ELISA kits (GZMB, 439207, BioLegend; IFNγ, 430101, BioLegend) following the manufacturer's protocols.

Evaluation of phosphorylation levels of CAR signalling domains

CAR T cells were prepared as previously described and collected at day 6 and day 10. CAR T cells were lysed with RIPA (P0013C, Beyotime) supplemented with a Complete EDTA-free protease inhibitor (4693132001, Roche) and PhosSTOP (04906845001, Roche) following the procedures described in the protocol. The antibodies used for immunoblotting were as follows: anti-CD3-ζ antibody (12837-2-AP, Proteintech) or an anti-pY142 CD3-ζ antibody (ab68235, Abcam). The membrane was recorded by the ChemiDoc XRS+ System (BIO-RAD).

Bulk RNA-seq analysis

CAR T cells and GSCs were incubated at a 1:4 effector cell ratio for 48 h before sorting. The cells were sorted as live CAR-positive cells and pelleted. Total mRNA was isolated from the CAR T cells and purified with the RNAeasy Animal Total RNA Isolation Kit (R0032, Beyotime) and then sequenced on a NovaSeq 6000 (Illumina) using a paired-end read 150-cycle kit. Salmon (v1.8.0)[58] software was used to quantify gene expression with default parameters. The DESeq2 (v1.30.1)[59] R package was used to calculate differences between conditions. Differentially expressed genes (DEGs) were identified as the genes with Bonferroni-adjusted *P* values less than 0.05 and $\log_2$(fold change) values greater than 1.

scRNA-seq analysis

Preparation and sequencing of scRNA-seq libraries were performed using the 10X Genomics Gene Expression Protocol (CG000331) as previously described. CAR T cells were isolated as described for the bulk RNA-seq analysis. At least 7,000 CAR T cells per sample were captured by a 10X Genomics machine. CAR T cell gene expression libraries were sequenced on the Illumina NovaSeq 6000 with a 150 bp paired-end read configuration. For gene expression libraries, 20,000 reads per cell were obtained. The raw sequencing data were processed using Cell Ranger (v5.0.0, 10X Genomics) software. The Seurat (v4.0.3)[60] R package was used to perform normalization, dimensionality reduction and differential expression analysis. The following criteria were applied to each sample to remove low-quality cells: gene number between 500 and 6,000, UMI count between 1,500 and 25,000, and mitochondrial content <10%. The cells that did not express CD3D or CD3E or that co-expressed CD8A and CD4 were removed. The DoubletFinder (v2.0.3)[61] method was used to predict doublets. After filtering, a total of 40,284 cells remained. Ribosomal and mitochondrial genes were excluded before downstream analysis. The batch effect across different samples was eliminated using Seurat's CCA method. The top 30 principal components were used to perform clustering and visualization. Finally, we obtained 12 clusters. DEGs were identified as the genes with Bonferroni-adjusted *P* values less than 0.05 and $\log_2$(fold change) values greater than 0.25.

CAR expression and stability assay

CAR T cell and tumour cells were cocultured in a 24-well plate at E:T = 1:4 and collected at indicated time points for flow cytometry and western blotting analysis. Surface protein was extracted by a membrane protein extraction kit following the procedures described in the protocol (89842, Thermo) and quantified by ImageJ software. The antibodies used for western blotting were as follows: anti-Myc tag antibody (9B11, Cell Signaling Technology) and anti-ATP1A1 antibody (14418-1-AP, Proteintech).

Immunoprecipitation

Binder or scFv CAR extracellular domains were overexpressed in GSC3565. Cells were collected and lysed by using RIPA Lysis Buffer (P0013C, Beyotime) following the procedures described in the protocol. Lysate was performed by overnight incubation with Anti-c-Myc Magnetic Beads (HY-K0206, MCE) on a rotor at 4 °C. The immunoprecipitates were eluted by loading buffer (E151-10, Genstar) at 100 °C for 10 min and analysed by immunoblotting. The antibodies used for immunoblotting were as follows: anti-Myc tag antibody (9B11, Cell Signaling Technology), anti-GAPDH antibody (60004-1-Ig, Proteintech), anti-EGFR antibody (2232, Cell Signaling Technology) and anti-CD276 antibody (ab134161, Abcam). The membrane was recorded by the ChemiDoc XRS+ System (BIO-RAD).

Surface CAR expression assay

CAR surface expression was recorded by stochastic optical reconstruction microscopy (STORM). About 0.5 million CAR T cells were seeded on the poly-L-lysine-coated coverslips (CG15XH, Thorlabs). Cells were fixed with 4% paraformaldehyde (50-980-487, Thermo) for 10 min. Cells were washed three times with PBS and stained with anti-Myc tag antibody (9B11, Cell Signaling Technology) for 1 h at room temperature. Samples were rinsed with PBS three times and stored in 1× PBS at 4 °C before imaging. The imaging buffer was made every time immediately before use, where catalase and glucose oxidase were diluted in base buffer (44% glycerol, 50 mM Tris pH 8.0, 10 mM NaCl, 10% glucose) with the addition of MEA (M6500-25G, Sigma-Aldrich). The final concentration of MEA was 35 mM. STORM imaging was performed on a custom-built super-resolution microscope using an oil objective (100×/1.5 NA, UPLAPO100XOHR, Olympus). All data were acquired under TIRF illumination at a 642 nm laser intensity of about 6.75 kW cm^{-2}. After image processing, the precise position of each fluorescent molecule in the image acquisition process was obtained. Cell boundaries were manually outlined according to fluorescent signals to obtain cell area. The number and density of localized molecules on the cell membrane were calculated by ImageJ. Since the preparation and imaging conditions were the same for all samples, the expression of CAR in different cells could be reflected by comparing the density of fluorescent molecules.

Imaging of cocultured cells

CAR T cells were cocultured with GSC3565 cells stably expressing the mCherry fluorescent protein at a 1:4 E:T ratio for 48 h. Images were acquired every 12 h using a fluorescence microscope (M5000, EVOS).

Animal experiments

All mouse experiments were performed under an animal protocol approved by the Institutional Animal Care and Use Committee of Westlake University and in accordance with the relevant guidelines (permission numbers 19-028-2-XQ). For the immunodeficient mouse model, luciferase-transduced GSCs were intracranially injected into individual NOD/SCID/IL2Rg$^{-/-}$ (NSG) mice (005557, JAX Lab). Ten days after tumour cell transplantation, the mice were intracranially treated with CAR T cells (1 million per mouse for EGFR CAR T cells). Body weight (g) and bioluminescence signals (photons/s) were recorded every 5 days after day 0. Bioluminescence imaging was performed by using an SI small animal imaging system (AMIHT, SI Imaging). To ensure statistical power, all groups included five mice. In parallel survival experiments, animals were monitored until they developed neurological signs. For evaluation of post-injected CAR T cells in vivo, tumour tissues were collected and dissociated at 1, 3 and 5 days after CAR T therapies with the Papain Dissociation System (LK003153, Worthington), and the tumour-infiltrating CAR T cells were analysed by flow cytometry. For the immunocompetent mouse model, 0.1 million GL261-hEGFR cells were intracranially injected into individual C57BL/6J mice (000664, JAX Lab). Seven days after tumour cell transplantation, the mice were intracranially treated with CAR T cells (2 million per mouse for EGFR CAR T cells). Body weight (g) was recorded every 5 days after day 0. To ensure statistical power, all groups included five mice. In parallel survival experiments, animals were monitored until they developed neurological signs. For examination for histological signs of pathological changes of CAR T-treated mice, organs were collected for haematoxylin and eosin (H&E) staining at 14 days after CAR T therapies.

Immunogenicity

C57BL/6 mice were treated every 3 days with 50 μg of EGFR binder or control (PBS) by intraperitoneal injection administration (6 times in total). Mice serum was collected at day 29, and anti-binder antibodies in serum were measured by ELISA. EGFR or CD276 binders were immobilized on Immuno Clear Standard Modules (468667, Thermo) at 2.5 μg ml^{-1} in 100 μl total volume per well and incubated at 4 °C overnight. Plates were blocked with 200 μl per well blocking buffer (TBS + 2% (w/v) BSA + 0.05% (v/v) Tween20) for 1 h at room temperature. Diluted sera samples (100 μl) (1:100) in blocking buffer were added to blocked wells. hEGFR-hFc (24,000 ng ml^{-1})/hCD276-hFc (240 ng ml^{-1}) in 100 μl of blocking buffer was used as a positive control. All samples were incubated for 1 h at room temperature. For the serum samples, 100 μl HRP-conjugated horse anti-mouse IgG antibody (1:5,000, #7076, Cell Signaling Technology) was incubated in each well at room temperature for 30 min. For the positive control, 100 μl HRP-conjugated mouse anti-human IgG antibody (1:500, #05-4220, Invitrogen) was incubated in each well at room temperature for 30 min. TMB (100 μl) (#SEKCR01, SWBIO) was added to each well at room temperature for 15 min. The reaction was quenched by adding 100 μl of Stop Solution for TMB Substrate (#P0215, Beyotime). The plates were washed 4 times with wash buffer (TBS + 0.1% (w/v) BSA + 0.05% (v/v) Tween20) between each step. Optical densities were determined at 450 nm on a Thermo Varioskan LUX Microplate reader (SIA-PR007, Thermo).

Target protein expression, purification and biotinylation

The gene of EGFR or CD276 protein was truncated and remained the extracellular domain (EGFR, residues ID 25–525, UniProt ID P00533; CD276, residues ID 107-320, UniProt ID A0A0C4DGH0). They were constructed on pCAG with an IgK secretory signal peptide (METDTLLLWVLLLWVPGSTG) on the N terminal and TEV cleavage site, 6× His-tag and BirA biotinylation tag (GSENLYFQGSHHHHHHGSGLNDIFEAQKIEWHE) on the C terminal. The target proteins were overexpressed in HEK293F cells with SMM 293-T II serum-free medium (M293TII, Sino Biological) at 37 °C in 5% CO_2. The plasmid was transfected with PEI when the cell density reached 1.0–2.0 × 10^6 cells per ml, and then cultured for 7 days. The cell culture medium was centrifuged at 12,000 rpm for 5 min and the target proteins were purified from the supernatant through Ni-NTA resin (30250, Qiagen) followed by size-exclusion chromatography (SEC) with a Superdex 200 Increase 10/300 GL (28990944, Cytiva) in PBS buffer (pH 8.0). The purified protein concentrations were determined by absorbance at 280 nm measured with a NanoPhotometer N50 (IMPLEN) using predicted extinction coefficients, then biotinylated with the BirA biotin-protein ligase standard reaction kit (BirA500, Avidity) following the manufacturer's protocol, and followed by SEC to remove the redundant biotin.

Yeast surface display

The *Saccharomyces cerevisiae* EBY100 strain was grown in SDCAA medium supplemented with 2% (w/v) glucose. For protein expression, yeast cells were transferred into SGCAA medium supplemented with 0.2% (w/v) glucose at a cell density of 0.3–0.5 × 10^7 cells per ml and induced at 30 °C and 200 rpm for 16 h. The yeast cells were centrifuged at 4,000 × *g* for 1 min and washed with PBSF buffer (PBS with 0.1% (w/v) BSA). The cells were incubated with biotinylated targets for 30 min, washed, labelled with anti-c-Myc fluorescein isothiocyanate (FITC, 130-116-653, Miltenyi Biotech) and streptavidin–phycoerythrin (SAPE, SA10044, Thermo Fisher) for 30 min, washed and analysed by flow cytometry. The final sorted pools were plated in SDCAA plates, and each individual clone was sequenced.

Mini-protein expression and purification

The genes encoding screened mini-protein binders were cloned into modified pET-28a (+) *E. coli* plasmid expression vectors with a 6× His-tag and thrombin cleavage site (MGSSHHHHHHSSGLVPRGS) in the N-terminus. The plasmids were transformed into chemically competent *E. coli* BL21 (DE3) cells (EC1002, WEIDIBio). The *E. coli* BL21 cells were grown in 1 l of Luria-Bertani (LB) broth at 37 °C until the density reached 0.6–0.8 at OD600. Then, IPTG (I104812, Aladdin) was added to the medium at a final concentration of 250 mM, and the *E. coli* cells were cultured at 37 °C overnight to overexpress the mini-binder. The cells were collected by centrifugation at 8,000 × *g* for 5 min, resuspended in protein buffer (25 mM Tris-HCL (pH 8.0) and 150 mM NaCl) and then lysed by ultrasonication for 10 min. The whole-cell lysates were clarified by centrifugation at 14,000 rpm for 30 min. The mini-protein binders were purified from the supernatant through Ni-NTA resin followed by SEC with a Superdex 75 Increase 10/300 GL (29148721, Cytiva) in PBS buffer (pH 8.0). The purified protein concentrations were determined with the Bradford Protein Assay Kit (P0006, Beyotime).

BLI

Protein–protein interactions were determined by BLI. BLI binding data were collected on an Octet RED96 (ForteBio) and processed by the instrument's integrated ForteBio Data Analysis software v.9.0.0.14. Biotinylated targets were loaded onto streptavidin-coated biosensors (18-5019, ForteBio) at 10 μg ml^{-1} in PBSM buffer (PBS with 0.5% (w/v) BSA) for 100 s (loading step) after baseline 1. Analyte proteins were dissolved in binding buffer to generate a concentration gradient. After baseline 2, the binding kinetics were monitored by dipping the biosensors in wells containing the mini-protein binders at the indicated concentration for 1,800 s (association step) and then dipping the sensors into binding buffer for 3,600 s (dissociation step). The maximum raw BLI binding signal was used as the indicator of binding strength. The maximum signal among all the mini-protein binders for a specific target was used to normalize the data for heatmap plotting.

Statistical analysis

Data analysis was performed using Prism version 9.0 (GraphPad Software), and data are presented as stated in individual figure legends. Comparisons were performed using two-way analysis of variance (ANOVA). Comparison of Kaplan–Meier survival data was performed using the log-rank (Mantel–Cox) test. The detailed comparisons in each experiment are described in the corresponding figure legend. Gene set enrichment analysis (GSEA) was performed by the GSEA desktop application (v4.1.0)[62]. The Seurat's Add Module Score function was used to calculate the signature score of the immune gene sets for a cluster. The signature scores of immune gene sets for each bulk sample were computed by the GSVA (v1.38.2)[63] R package with method = 'gsva'.

Reporting summary

Further information on research design is available in the Nature Portfolio Reporting Summary linked to this article.

Data availability

All raw sequencing data and selected processed datasets are available from the NCBI Sequence Read Archive under the accession number PRJNA935143. The raw and analysed datasets generated during the study are available for research purposes from the corresponding authors on reasonable request. Source data are provided with this paper.

Code availability

Analytic codes used to generate figures that support the findings of this study will be available from the corresponding authors upon reasonable request.

References

1. Wu, W. et al. Glioblastoma multiforme (GBM): an overview of current therapies and mechanisms of resistance. *Pharmacol. Res.* **171**, 105780 (2021).

2. Maher, E. A. et al. Malignant glioma: genetics and biology of a grave matter. *Genes Dev.* **15**, 1311–1333 (2001).
3. Bovenberg, M. S., Degeling, M. H. & Tannous, B. A. Cell-based immunotherapy against gliomas: from bench to bedside. *Mol. Ther.* **21**, 1297–1305 (2013).
4. Jackson, C. M., Choi, J. & Lim, M. Mechanisms of immunotherapy resistance: lessons from glioblastoma. *Nat. Immunol.* **20**, 1100–1109 (2019).
5. Sampson, J. H., Maus, M. V. & June, C. H. Immunotherapy for brain tumors. *J. Clin. Oncol.* **35**, 2450–2456 (2017).
6. Samaha, H. et al. A homing system targets therapeutic T cells to brain cancer. *Nature* **561**, 331–337 (2018).
7. Migliorini, D. et al. CAR T-cell therapies in glioblastoma: a first look. *Clin. Cancer Res.* **24**, 535–540 (2018).
8. Neelapu, S. S. et al. Axicabtagene ciloleucel CAR T-cell therapy in refractory large B-cell lymphoma. *N. Engl. J. Med.* **377**, 2531–2544 (2017).
9. Maude, S. L. et al. Tisagenlecleucel in children and young adults with B-cell lymphoblastic leukemia. *N. Engl. J. Med.* **378**, 439–448 (2018).
10. Schuster, S. J. et al. Chimeric antigen receptor T cells in refractory B-cell lymphomas. *N. Engl. J. Med.* **377**, 2545–2554 (2017).
11. Quail, D. F. & Joyce, J. A. Microenvironmental regulation of tumor progression and metastasis. *Nat. Med.* **19**, 1423–1437 (2013).
12. Yin, Y. et al. Checkpoint blockade reverses anergy in IL-13Ralpha2 humanized scFv-based CAR T cells to treat murine and canine gliomas. *Mol. Ther. Oncolytics* **11**, 20–38 (2018).
13. Grosser, R., Cherkassky, L., Chintala, N. & Adusumilli, P. S. Combination immunotherapy with CAR T cells and checkpoint blockade for the treatment of solid tumors. *Cancer Cell* **36**, 471–482 (2019).
14. Abreu, T. R., Fonseca, N. A., Goncalves, N. & Moreira, J. N. Current challenges and emerging opportunities of CAR-T cell therapies. *J. Control. Release* **319**, 246–261 (2020).
15. Wang, D. et al. CRISPR screening of CAR T cells and cancer stem cells reveals critical dependencies for cell-based therapies. *Cancer Discov.* **11**, 1192–1211 (2021).
16. Carnevale, J. et al. RASA2 ablation in T cells boosts antigen sensitivity and long-term function. *Nature* **609**, 174–182 (2022).
17. Ye, L. et al. A genome-scale gain-of-function CRISPR screen in CD8 T cells identifies proline metabolism as a means to enhance CAR-T therapy. *Cell Metab.* **34**, 595–614 e514 (2022).
18. Gomes-Silva, D. et al. Tonic 4-1BB costimulation in chimeric antigen receptors impedes T cell survival and is vector-dependent. *Cell Rep.* **21**, 17–26 (2017).
19. Long, A. H. et al. 4-1BB costimulation ameliorates T cell exhaustion induced by tonic signaling of chimeric antigen receptors. *Nat. Med.* **21**, 581–590 (2015).
20. Ajina, A. & Maher, J. Strategies to address chimeric antigen receptor tonic signaling. *Mol. Cancer Ther.* **17**, 1795–1815 (2018).
21. Morgan, M. A. & Schambach, A. Engineering CAR-T cells for improved function against solid tumors. *Front. Immunol.* **9**, 2493 (2018).
22. Larson, R. C. & Maus, M. V. Recent advances and discoveries in the mechanisms and functions of CAR T cells. *Nat. Rev. Cancer* **21**, 145–161 (2021).
23. Jayaraman, J. et al. CAR-T design: elements and their synergistic function. *eBioMedicine* **58**, 102931 (2020).
24. Chevalier, A. et al. Massively parallel de novo protein design for targeted therapeutics. *Nature* **550**, 74–79 (2017).
25. Silva, D. A. et al. De novo design of potent and selective mimics of IL-2 and IL-15. *Nature* **565**, 186–191 (2019).
26. Cao, L. et al. De novo design of picomolar SARS-CoV-2 miniprotein inhibitors. *Science* **370**, 426–431 (2020).
27. Cao, L. et al. Design of protein-binding proteins from the target structure alone. *Nature* **605**, 551–560 (2022).
28. Park, J. S. et al. Isoform-specific inhibition of FGFR signaling achieved by a de-novo-designed mini-protein. *Cell Rep.* **41**, 111545 (2022).
29. Case, J. B. et al. Ultrapotent miniproteins targeting the SARS-CoV-2 receptor-binding domain protect against infection and disease. *Cell Host Microbe* **29**, 1151–1161 e1155 (2021).
30. Liu, Y. et al. Anti-EGFR chimeric antigen receptor-modified T cells in metastatic pancreatic carcinoma: a phase I clinical trial. *Cytotherapy* **22**, 573–580 (2020).
31. Gimple, R. C., Bhargava, S., Dixit, D. & Rich, J. N. Glioblastoma stem cells: lessons from the tumor hierarchy in a lethal cancer. *Genes Dev.* **33**, 591–609 (2019).
32. Chen, J. et al. Tuning charge density of chimeric antigen receptor optimizes tonic signaling and CAR-T cell fitness. *Cell Res.* **33**, 341–354 (2023).
33. Landoni, E. et al. Modifications to the framework regions eliminate chimeric antigen receptor tonic signaling. *Cancer Immunol. Res.* **9**, 441–453 (2021).
34. Walker, A. J. et al. Tumor antigen and receptor densities regulate efficacy of a chimeric antigen receptor targeting anaplastic lymphoma kinase. *Mol. Ther.* **25**, 2189–2201 (2017).
35. Li, W. et al. Chimeric antigen receptor designed to prevent ubiquitination and downregulation showed durable antitumor efficacy. *Immunity* **53**, 456–470 e456 (2020).
36. Davenport, A. J. et al. CAR-T cells inflict sequential killing of multiple tumor target cells. *Cancer Immunol. Res.* **3**, 483–494 (2015).
37. Sharma, P. et al. Structure-guided engineering of the affinity and specificity of CARs against Tn-glycopeptides. *Proc. Natl Acad. Sci. USA* **117**, 15148–15159 (2020).
38. Olson, M. L. et al. Low-affinity CAR T cells exhibit reduced trogocytosis, preventing rapid antigen loss, and increasing CAR T cell expansion. *Leukemia* **36**, 1943–1946 (2022).
39. Zhang, J. et al. B7H3 regulates differentiation and serves as a potential biomarker and theranostic target for human glioblastoma. *Lab. Invest.* **99**, 1117–1129 (2019).
40. Du, H. et al. Antitumor responses in the absence of toxicity in solid tumors by targeting B7-H3 via chimeric antigen receptor T cells. *Cancer Cell* **35**, 221–237 e228 (2019).
41. Nehama, D. et al. B7-H3-redirected chimeric antigen receptor T cells target glioblastoma and neurospheres. *eBioMedicine* **47**, 33–43 (2019).
42. Sterner, R. C. & Sterner, R. M. CAR-T cell therapy: current limitations and potential strategies. *Blood Cancer J.* **11**, 69 (2021).
43. Quijano-Rubio, A. et al. A split, conditionally active mimetic of IL-2 reduces the toxicity of systemic cytokine therapy. *Nat. Biotechnol.* https://doi.org/10.1038/s41587-022-01510-z (2022).
44. Liu, X. et al. Affinity-tuned ErbB2 or EGFR chimeric antigen receptor T cells exhibit an increased therapeutic index against tumors in mice. *Cancer Res.* **75**, 3596–3607 (2015).
45. Drent, E. et al. A rational strategy for reducing on-target off-tumor effects of CD38-chimeric antigen receptors by affinity optimization. *Mol. Ther.* **25**, 1946–1958 (2017).
46. Arcangeli, S. et al. Balance of anti-CD123 chimeric antigen receptor binding affinity and density for the targeting of acute myeloid leukemia. *Mol. Ther.* **25**, 1933–1945 (2017).
47. Ahmad, Z. A. et al. scFv antibody: principles and clinical application. *Clin. Dev. Immunol.* **2012**, 980250 (2012).
48. Xiao, Q. et al. Size-dependent activation of CAR-T cells. *Sci. Immunol.* **7**, eabl3995 (2022).
49. Caruso, H. G. et al. Tuning sensitivity of CAR to EGFR density limits recognition of normal tissue while maintaining potent antitumor activity. *Cancer Res.* **75**, 3505–3518 (2015).

50. Eyquem, J. et al. Targeting a CAR to the TRAC locus with CRISPR/Cas9 enhances tumour rejection. *Nature* **543**, 113–117 (2017).
51. Hamieh, M. et al. CAR T cell trogocytosis and cooperative killing regulate tumour antigen escape. *Nature* **568**, 112–116 (2019).
52. Li, H. et al. Antitumor activity of EGFR-specific CAR T cells against non-small-cell lung cancer cells in vitro and in mice. *Cell Death Dis.* **9**, 177 (2018).
53. Zhang, Y. et al. Phase I clinical trial of EGFR-specific CAR-T cells generated by the piggyBac transposon system in advanced relapsed/refractory non-small cell lung cancer patients. *J. Cancer Res. Clin. Oncol.* **147**, 3725–3734 (2021).
54. Zhang, Z. et al. B7-H3-targeted CAR-T cells exhibit potent antitumor effects on hematologic and solid tumors. *Mol. Ther. Oncolytics* **17**, 180–189 (2020).
55. Li, D. et al. Camel nanobody-based B7-H3 CAR-T cells show high efficacy against large solid tumours. *Nat. Commun.* **14**, 5920 (2023).
56. Li, L. et al. GFAP mutations in astrocytes impair oligodendrocyte progenitor proliferation and myelination in an hiPSC model of Alexander disease. *Cell Stem Cell* **23**, 239–251 e236 (2018).
57. Zhou, Y. et al. Prokaryotic expression and refolding of EGFR extracellular domain and generation of phage display human scFv against EGFR. *Biomed. Pharmacother.* **67**, 737–743 (2013).
58. Patro, R., Duggal, G., Love, M. I., Irizarry, R. A. & Kingsford, C. Salmon provides fast and bias-aware quantification of transcript expression. *Nat. Methods* **14**, 417–419 (2017).
59. Love, M. I., Huber, W. & Anders, S. Moderated estimation of fold change and dispersion for RNA-seq data with DESeq2. *Genome Biol.* **15**, 550 (2014).
60. Hao, Y. et al. Integrated analysis of multimodal single-cell data. *Cell* **184**, 3573–3587 e3529 (2021).
61. McGinnis, C. S., Murrow, L. M. & Gartner, Z. J. DoubletFinder: doublet detection in single-cell RNA sequencing data using artificial nearest neighbors. *Cell Syst.* **8**, 329–337 e324 (2019).
62. Subramanian, A. et al. Gene set enrichment analysis: a knowledge-based approach for interpreting genome-wide expression profiles. *Proc. Natl Acad. Sci. USA* **102**, 15545–15550 (2005).
63. Hanzelmann, S., Castelo, R. & Guinney, J. GSVA: gene set variation analysis for microarray and RNA-seq data. *BMC Bioinf.* **14**, 7 (2013).

Acknowledgements

We thank H. Wakimoto (Massachusetts General Hospital) for kindly providing the MGG4 and MGG6 GSC lines. We thank H. Yu (Westlake University) and D. Baker (University of Washington) for providing helpful discussions. We thank the Core Facilities at the Center for Biomedical Research of Westlake University for sample analysis. This work was supported by grants from the National Natural Science Foundation of China (82073268) and Westlake Education Foundation to Q.X., Science and Technology Innovation 2030 Major Project (2021ZD0150100), the National Key R&D Program of China (2021YFC2301401 and 2022YFA1303700), National Natural Science Foundation of China (32370989) and Westlake Education Foundation to L.C. We also thank the Research Center for Industries of the Future (RCIF) at Westlake University (210210006022210) and 'Pioneer' and 'Leading Goose' R&D Program of Zhejiang (2024SSYS0036) for supporting this work.

Author contributions

Z.X., Q.J., Z.L., Y.H., C.S., J.L., Chentong Wang, W.Z. and T.Z. performed or assisted with the experiments. Z.X., Q.J., Z.L., Y.H., C.S., J.L., Chentong Wang, W.Z. and T.Z. analysed the data and supported the project. F.L., Chun Wang and J.Z. provided critical reagents. Y.Z., L.C. and Q.X. supervised the project and acquired the funding. Z.X., Q.J., L.C. and Q.X. designed the experiments. J.N.R. provided the 3565 GSC cell line and helped with the paper editing. Z.X., Q.J., L.C. and Q.X. wrote the paper. All authors critically read and approved the final paper.

Competing interests

Westlake University has submitted a patent application for the de novo-designed CD276 binders (patent number: PCT/CN2023/140615). The other authors declare no competing interests.

Additional information

Extended data is available for this paper at https://doi.org/10.1038/s41551-024-01258-8.

Supplementary information The online version contains supplementary material available at https://doi.org/10.1038/s41551-024-01258-8.

Correspondence and requests for materials should be addressed to Longxing Cao or Qi Xie.

Peer review information *Nature Biomedical Engineering* thanks Donald O'Rourke and the other, anonymous, reviewer(s) for their contribution to the peer review of this work. Peer reviewer reports are available.

https://doi.org/10.1038/s41551-024-01258-8

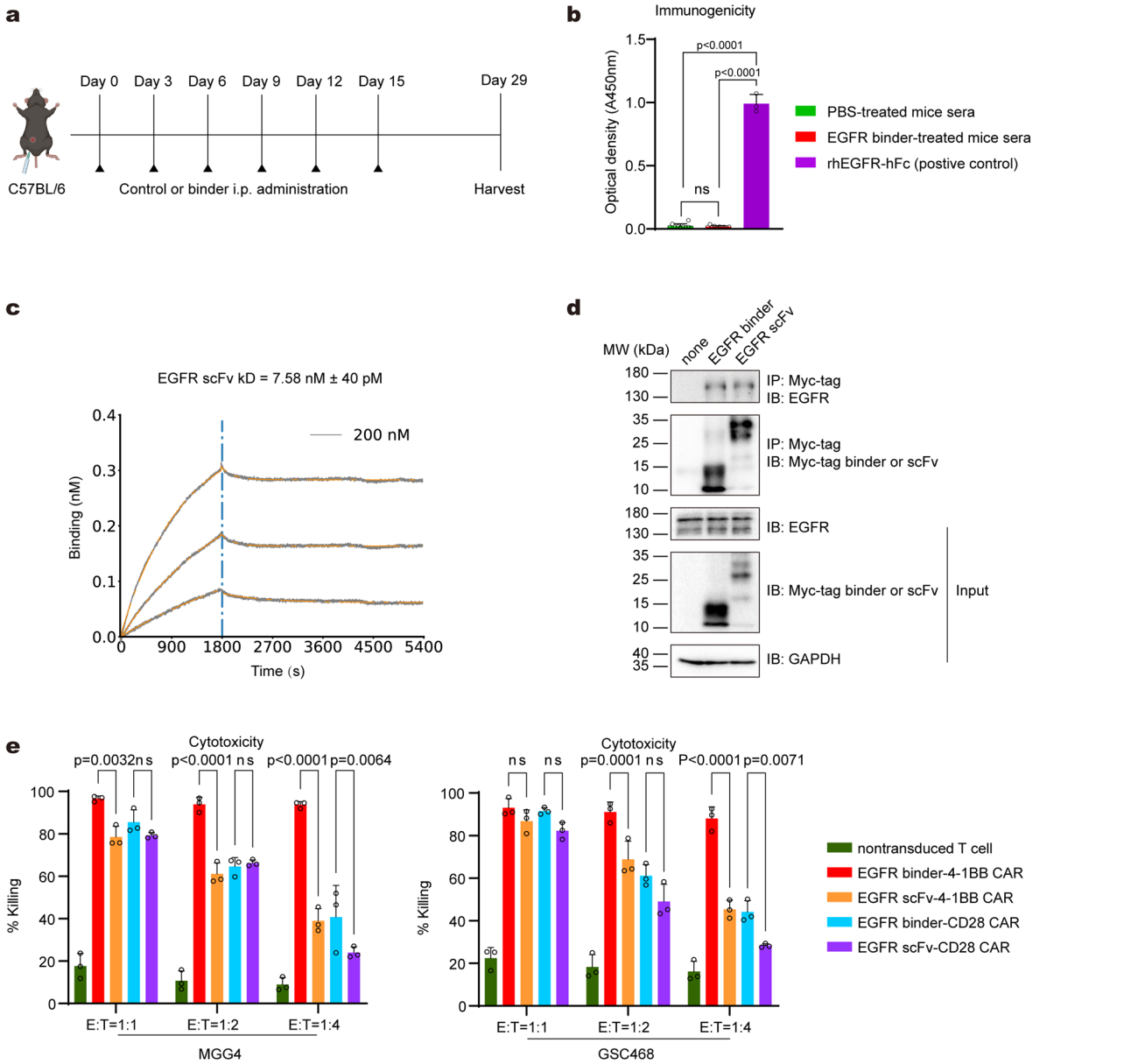

Extended Data Fig. 1 | Evaluation of EGFR binder CAR T cell cytotoxicity to different GSCs. a, Scheme of experimental details. C57BL/6 mice (n = 10 per group) were treated every 3 days with 50 μg of EGFR binder or control (PBS) by i.p. administration (6 times in total). Mice serum was harvested at day 29, and anti-binder antibodies in serum were measured by ELISA. **b**, Binding of serum antibodies to EGFR binder as measured by ELISA. rhEGFR-hFc serves as positive control. Data are shown as the mean ± SD (ANOVA; ns: not significant; mouse serum: n = 10, positive control: n = 3). **c**, Biolayer interferometry characterization of the binding of the EGFR scFv to EGFR. Biotinylated EGFR proteins were loaded onto streptavidin (SA) biosensors and incubated with protein binders in solution to measure association and dissociation. Twofold serial dilutions were tested for each binder, and the highest concentration was labeled. The gray curves represent experimental data, and the orange curves represent fit curves. **d**, Representative immunoblot analysis of immunoprecipitation of EGFR binder and scFv. **e**, Percent tumor killing activity of the indicated CAR T cells against cocultured MGG4 and GSC468 cells at different E:T ratios. Data are displayed as the mean ± SD (ANOVA; ns: not significant; n = 3).

https://doi.org/10.1038/s41551-024-01258-8

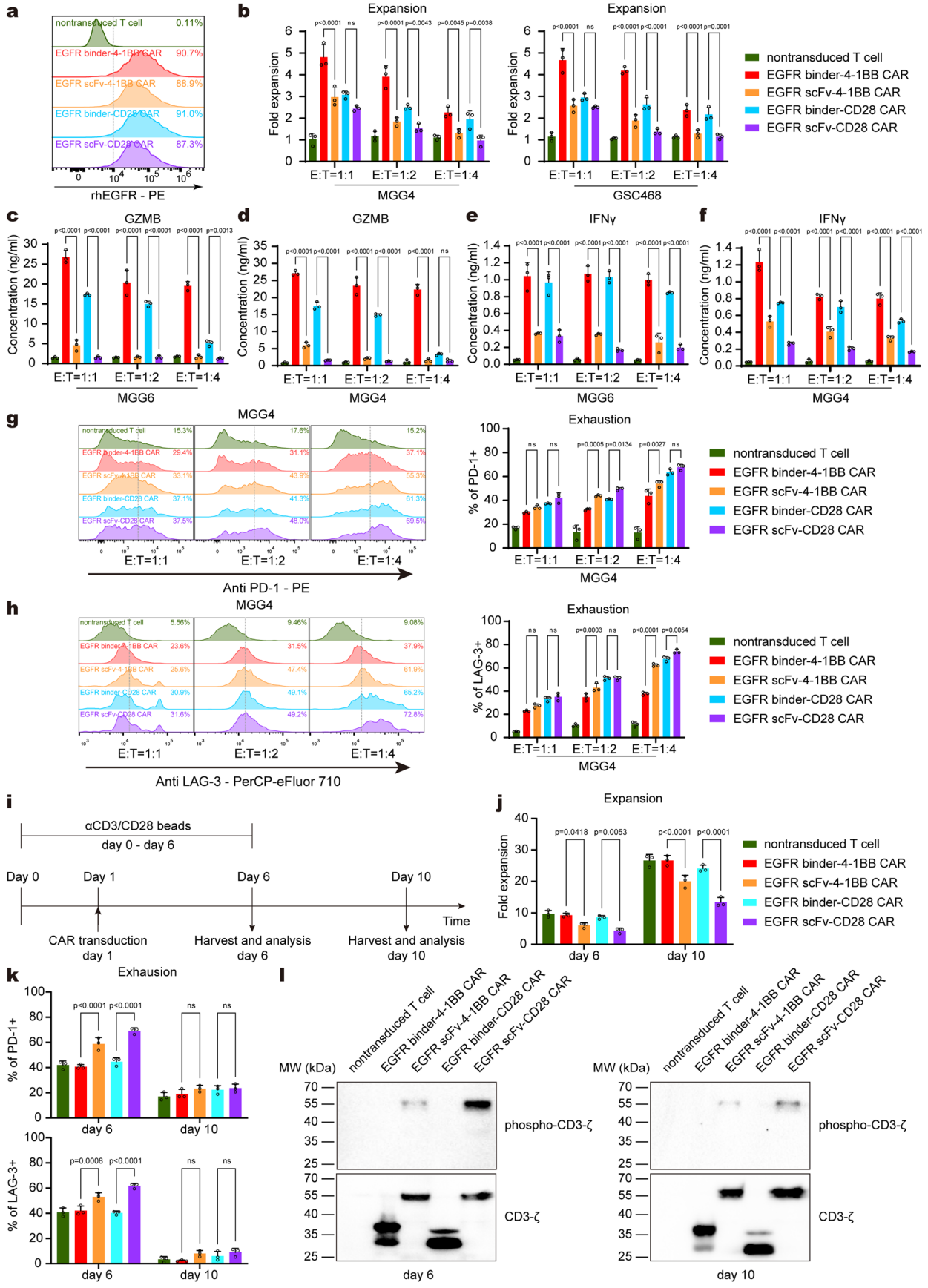

Extended Data Fig. 2 | See next page for caption.

https://doi.org/10.1038/s41551-024-01258-8

Extended Data Fig. 2 | EGFR binder CAR T cells exhibited improved effector potency against GSCs. a, CAR expression was determined by staining for the rhEGFR-PE**. b**, Expansion evaluation of the indicated CAR T cells in cocultures with MGG4 and GSC468 cells at gradient E:T ratios. Data are displayed as the mean ± SD (ANOVA; ns: not significant; n = 3). **c**-**d**, Evaluation of GZMB secretion by the indicated CAR T cells in cocultures with MGG6 (**c**) or MGG4 (**d**) cells at gradient E:T ratios. Data are displayed as the mean ± SD (ANOVA; ns: not significant; n = 3). **e**-**f**, Evaluation of IFNγ secretion by the indicated CAR T cells in cocultures with MGG6 (**E**) or MGG4 (**F**) cells at gradient E:T ratios. Data are displayed as the mean ± SD (ANOVA; ns: not significant; n = 3). **g**, The expression of the exhaustion marker PD-1 in the indicated CAR T cells was measured after coculture with MGG4 cells at gradient E:T ratios for 48 h. Data are represented as the mean ± SD (ANOVA; ns: not significant; n = 3). **h**, The expression of the exhaustion marker LAG-3 in the indicated CAR T cells was measured after coculture with MGG4 cells at gradient E:T ratios for 48 h. Data are represented as the mean ± SD (ANOVA; ns: not significant; n = 3). **i**, Scheme of experimental details. PBMCs from healthy donors were activated with αCD3/CD28 T cell Activation Dynabeads (cell: beads = 1:1) for 6 days. On day 1 post activation, T cells were transduced with CAR lentivirus. Activation Dynabeads were removed at day 6. **j**-**k**, expansion (**j**) and exhaustion (**k**) evaluations of the indicated CAR T cells without antigen stimulation. Data are shown as the mean ± SD (ANOVA; n = 3). **l**, Western blot evaluating phosphorylation levels of CAR signaling domains using anti-phospho-CD3-ζ and anti-CD3-ζ, respectively. T cells from each group were evaluated on day 6 and day 10 after initial activation. Basal phosphorylation was evaluated without further stimulation.

https://doi.org/10.1038/s41551-024-01258-8

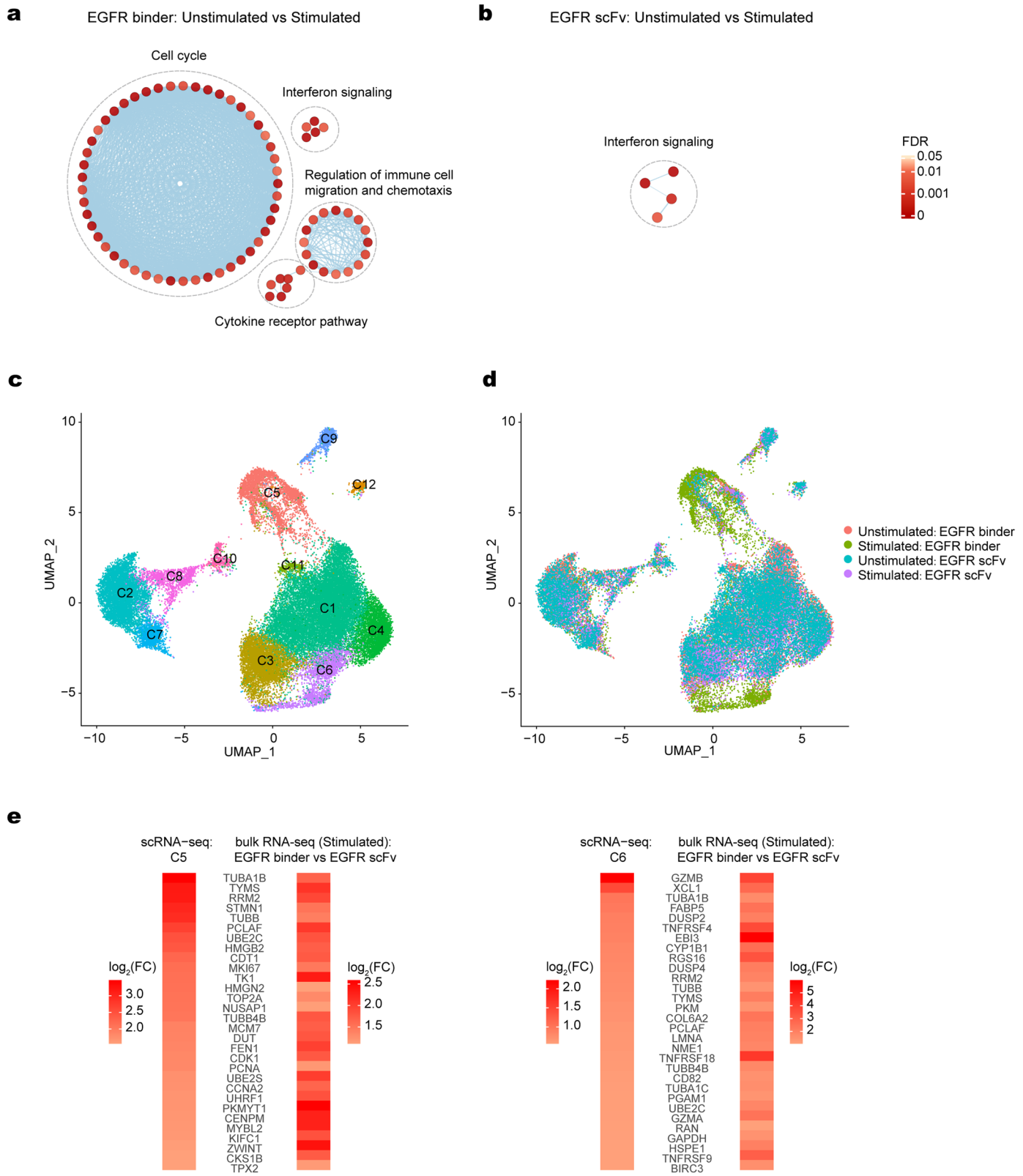

Extended Data Fig. 3 | Transcriptional profiling of EGFR binder and EGFR scFv CAR T cells. a, Signaling pathways significantly enriched in EGFR binder CAR T cells after stimulation with GSCs. **b**, Signaling pathways significantly enriched in EGFR scFv CAR T cells after stimulation with GSCs. **c**-**d**, UMAP plot of single-cell RNA-seq data for EGFR binder and EGFR scFv CAR T cells both before and after stimulation with GSCs. **e**, The top 30 marker genes of clusters C5 and C6, identified from single-cell RNA-seq, were consistently upregulated in EGFR binder CAR T cells as shown by bulk RNA-seq data.

https://doi.org/10.1038/s41551-024-01258-8

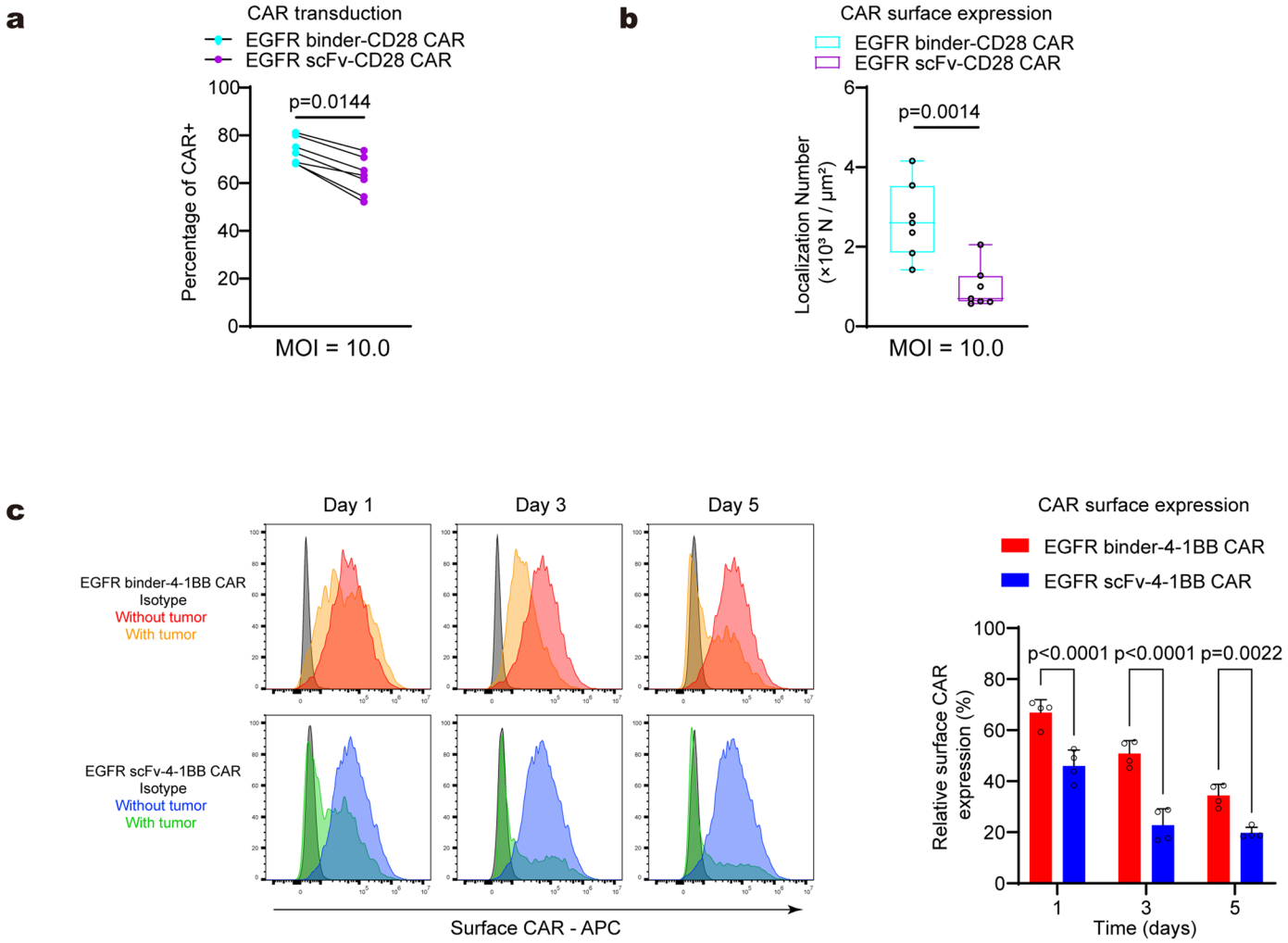

Extended Data Fig. 4 | The binder CAR improved the efficiency of CAR transduction and enhanced CAR stability in vivo. a, The percentage of CAR transduction is shown for paired samples of EGFR binder-CD28 CAR T and EGFR scFv-CD28 CAR T cells (paired t-test; n = 7). **b**, CAR surface expression (Localization Number / Area (N / μm²)) is counted by stochastic optical reconstruction microscopy (STORM) imaging. STORM imaging was performed on a custom-built super-resolution microscope using an oil objective (100× 1.5NA, UPLAPO100XOHR, Olympus), and it is analyzed by imageJ software. The boxes depicted the upper and lower quartiles of the data, while the whiskers represented the entire range of points, from the minimum to the maximum values (paired t-test; n = 7). **c**, Harvest and digest tumor tissues at 1, 3, 5 days after CAR T therapies, and surface CAR expression level of tumor infiltrated CAR T cells was measured by flowcytometry. Mean fluorescence intensity (MFI) was obtained to calculate percentage of surface CAR degradation in EGFR binder and EGFR scFv CAR T cells (ANOVA; n = 4).

https://doi.org/10.1038/s41551-024-01258-8

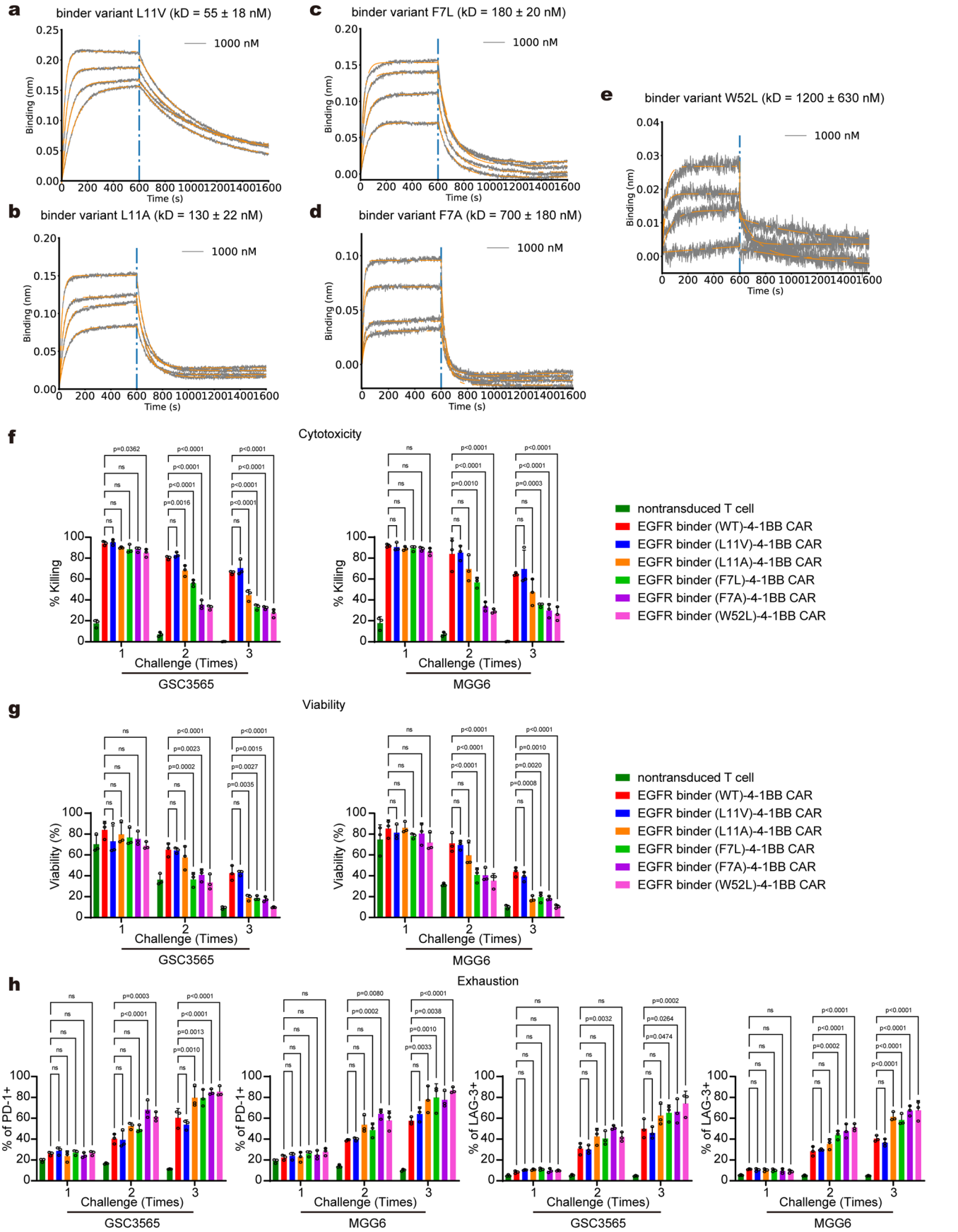

Extended Data Fig. 5 | EGFR binder CAR has a certain affinity window for tumor targeting. a-e, Biolayer interferometry characterization of the binding of the EGFR binder variants L11V (**a**), L11A (**b**), F7L (**c**), F7A (**d**), and W52L (**e**) to EGFR. **f-h**, Cytotoxicity (**h**), cell viability (**g**) and exhaustion (**h**) evaluations of the indicated CAR T cells with multiple rounds of tumor challenging (E:T = 1:1 for 48 h per round). Data are shown as the mean ± SD (ANOVA; ns: not significant; n = 3).

https://doi.org/10.1038/s41551-024-01258-8

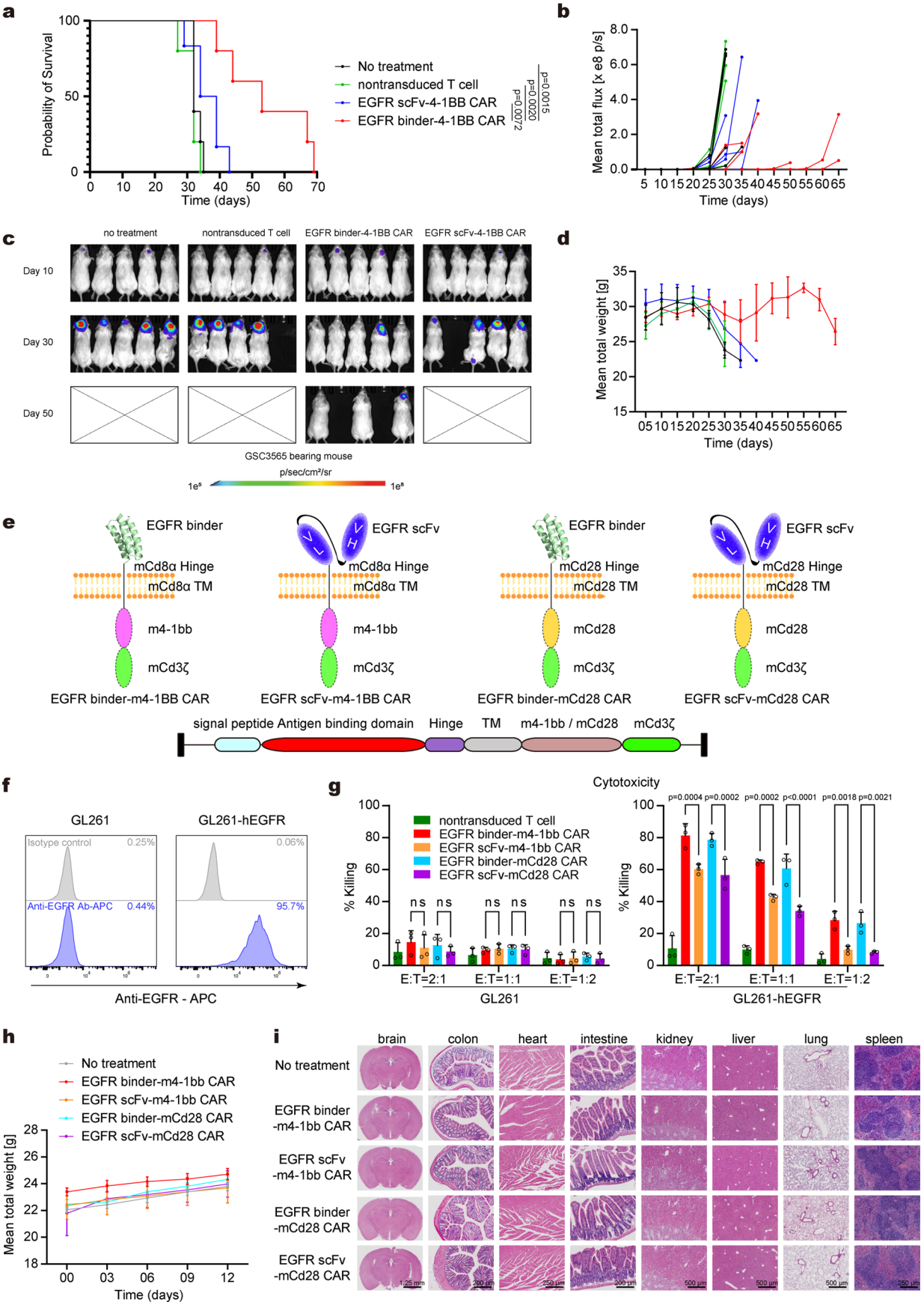

Extended Data Fig. 6 | See next page for caption.

https://doi.org/10.1038/s41551-024-01258-8

Extended Data Fig. 6 | EGFR binder CAR T cells inhibit tumor growth in vivo. a, Kaplan–Meier survival curves of mice bearing intracranial GSC3565 cells treated with control T cells, EGFR binder-4-1BB CAR T cells or EGFR scFv-4-1BB CAR T cells. P values were calculated using the log-rank test (n = 5). **b-c**, Bioluminescence imaging to measure GSC3565 tumor cell growth in vivo. **d**, Body weight measurement of mice in the indicated treatment groups. **e**, Diagram of the indicated mouse CAR structures. **f**, hEGFR expression on GL261 and GL261-hEGFR was measured by anti-EGFR antibody flow cytometric staining. **g**, Percent tumor killing activity of the indicated CAR T cells against cocultured tumor cells. Data are represented as the mean ± SD (ANOVA; ns: not significant; n = 3). **h**, 2 million CAR T cells were intracranial injected in mice at day 0. After injection, the body weight of the mice was measured every three days (n = 3). **i**, Representative H&E staining of mice in the indicated treatment groups.

https://doi.org/10.1038/s41551-024-01258-8

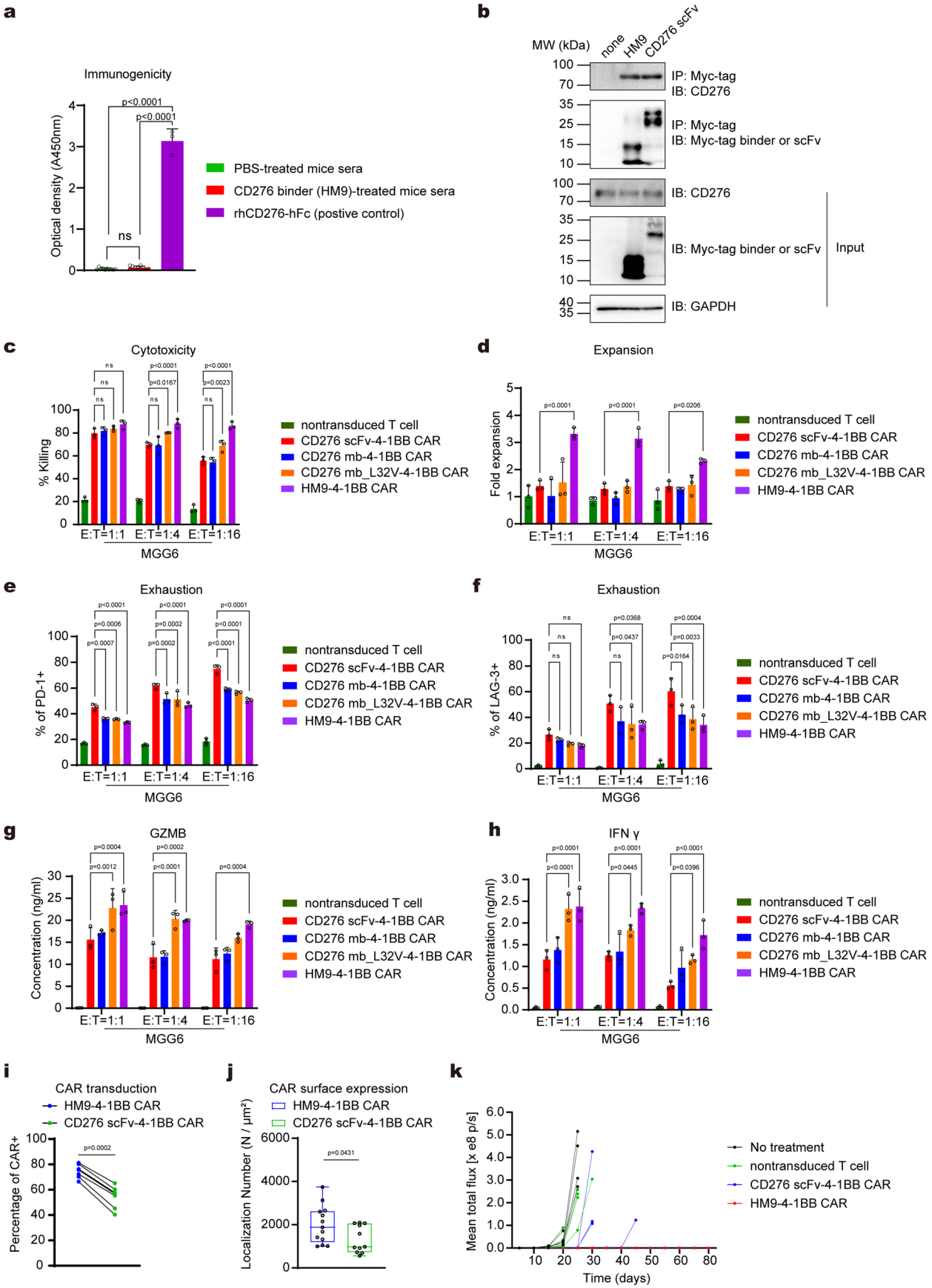

Extended Data Fig. 7 | See next page for caption.

https://doi.org/10.1038/s41551-024-01258-8

Extended Data Fig. 7 | CD276 binder CAR T cells exhibited enhanced effector potency. a, Binding of serum antibodies to CD276 binder (HM9) as measured by ELISA. rhCD276-hFc serves as positive control. Data are shown as the mean ± SD (ANOVA; ns: not significant; mouse serum: n = 10, positive control: n = 3). **b**, Representative immunoblot analysis of immunoprecipitation of CD276 binder (HM9) and CD276 scFv. **c**-**h**, Cytotoxicity (**c**), expansion (**d**), PD-1 expression (**e**), LAG-3 expresison (**f**), GZMB secretion (**g**) and IFNγ secretion (**h**) evaluations of the indicated CAR T cells in cocultures with GSC3565 at gradient E:T ratios. Data are displayed as the mean ± SD (ANOVA; ns: not significant; n = 3). **i**, CAR transduction (percentage of CAR) is shown for paired samples of HM9 CAR and CD276 scFv CAR from 7 independent T cell lots (paired t-test; n = 7). **j**, CAR surface expression (Localization Number / Area (N / μm^2)) is counted by stochastic optical reconstruction microscopy (STORM) imaging. STORM imaging was performed on a custom-built super-resolution microscope using an oil objective (100× 1.5NA, UPLAPO100XOHR, Olympus),and it is analyzed by imageJ software. The boxes depicted the upper and lower quartiles of the data, while the whiskers represented the entire range of points, from the minimum to the maximum values (paired t-test; n = 13, 11). **k**, Bioluminescence imaging to measure GSC3565 tumor cell growth in vivo.

nature portfolio

Corresponding author(s): Qi Xie

Last updated by author(s): May 21, 2024

Reporting Summary

Nature Portfolio wishes to improve the reproducibility of the work that we publish. This form provides structure for consistency and transparency in reporting. For further information on Nature Portfolio policies, see our Editorial Policies and the Editorial Policy Checklist.

Statistics

For all statistical analyses, confirm that the following items are present in the figure legend, table legend, main text, or Methods section.

n/a	Confirmed	
☐	☒	The exact sample size (*n*) for each experimental group/condition, given as a discrete number and unit of measurement
☐	☒	A statement on whether measurements were taken from distinct samples or whether the same sample was measured repeatedly
☐	☒	The statistical test(s) used AND whether they are one- or two-sided *Only common tests should be described solely by name; describe more complex techniques in the Methods section.*
☒	☐	A description of all covariates tested
☐	☒	A description of any assumptions or corrections, such as tests of normality and adjustment for multiple comparisons
☐	☒	A full description of the statistical parameters including central tendency (e.g. means) or other basic estimates (e.g. regression coefficient) AND variation (e.g. standard deviation) or associated estimates of uncertainty (e.g. confidence intervals)
☐	☒	For null hypothesis testing, the test statistic (e.g. *F*, *t*, *r*) with confidence intervals, effect sizes, degrees of freedom and *P* value noted *Give P values as exact values whenever suitable.*
☒	☐	For Bayesian analysis, information on the choice of priors and Markov chain Monte Carlo settings
☐	☒	For hierarchical and complex designs, identification of the appropriate level for tests and full reporting of outcomes
☒	☐	Estimates of effect sizes (e.g. Cohen's *d*, Pearson's *r*), indicating how they were calculated

Our web collection on statistics for biologists contains articles on many of the points above.

Software and code

Policy information about availability of computer code

Data collection	CAR T cells and GSCs were incubated at a 1:4 effector cell ratio for 48 hours prior to sorting. The cells were sorted as live CAR-positive cells and pelleted. Total mRNA was isolated from the CAR T cells and purified with the RNAeasy Animal Total RNA Isolation Kit (R0032, Beyotime) and then sequenced on a NovaSeq 6000 (Illumina) using a paired-end reads 150-cycle kit. Preparation and sequencing of scRNA-seq libraries were performed using the 10X Genomics Gene Expression Protocol (CG000331) as previously described. CAR T cells were isolated as described for the bulk RNA-seq analysis. At least 7,000 CAR T cells per sample were captured by a 10X Genomics machine. CAR T cell gene expression libraries were sequenced on the Illumina NovaSeq 6000 platform with a 150-bp paired-end read configuration.
Data analysis	RNA-seq, scRNA-seq, and GSEA analysis: Salmon v1.8.0, DESeq2 v1.30.1 package, Cell Ranger v5.0.0, Seurat v4.0.3 package, DoubletFinder v2.0.3 package, GSEA v4.1.0, GSVA v1.38.2 package. Flow cytometry analysis: FlowJo v.10 (Tree Star, Inc), Prism 9 (GraphPad Software) Tumor growth curve / survival curve analysis: Prism 9 (GraphPad Software) Assembly / layout of figures: Adobe Illustrator 2019

For manuscripts utilizing custom algorithms or software that are central to the research but not yet described in published literature, software must be made available to editors and reviewers. We strongly encourage code deposition in a community repository (e.g. GitHub). See the Nature Portfolio guidelines for submitting code & software for further information.

Data

Policy information about availability of data

All manuscripts must include a data availability statement. This statement should provide the following information, where applicable:

- Accession codes, unique identifiers, or web links for publicly available datasets
- A description of any restrictions on data availability
- For clinical datasets or third party data, please ensure that the statement adheres to our policy

All raw sequencing data and selected processed datasets are available from the NCBI Sequence Read Archive under the accession number PRJNA935143. Source data for the figures are provided with this paper. The raw and analysed datasets generated during the study are available for research purposes from the corresponding authors on reasonable request.

Research involving human participants, their data, or biological material

Policy information about studies with human participants or human data. See also policy information about sex, gender (identity/presentation), and sexual orientation and race, ethnicity and racism.

Reporting on sex and gender	Sex and gender were not considered in this study design.
Reporting on race, ethnicity, or other socially relevant groupings	Glioblastoma primary cells were obtained from excess surgical resection samples from patients at The Second Affiliated Hospital Zhejiang University School of Medicine with appropriate consent and in accordance with an IRB-approved protocol (NO. IR2022453).
Population characteristics	GBM_12388157: male, 48 years old， IDH WT; GBM_12479390: male, 67 years old,IDH WT.
Recruitment	No selection had been made, and the recruitment and collection of human samples were conducted in accordance with approved IRB protocols.
Ethics oversight	This study was conducted in accordance with the Declaration of Helsinki and was approved by the Second Affiliated Hospital of Zhejiang University School of Medicine. Prior to participation, written informed consent was obtained from all patients involved in the study.

Note that full information on the approval of the study protocol must also be provided in the manuscript.

Field-specific reporting

Please select the one below that is the best fit for your research. If you are not sure, read the appropriate sections before making your selection.

☒ Life sciences ☐ Behavioural & social sciences ☐ Ecological, evolutionary & environmental sciences

For a reference copy of the document with all sections, see nature.com/documents/nr-reporting-summary-flat.pdf

Life sciences study design

All studies must disclose on these points even when the disclosure is negative.

Sample size	Sample sizes were not predetermined statistically but were chosen on the basis of previous research in GBM tumour formation assays (PMID: 28678782 Nature 2017; PMID: 30392959 Cell 2018) and tumour immunology (PMID: 32879489 Nature 2020; PMID: 33328215 Cancer Discovery 2021). Group sizes for in vivo experiments were selected empirically on the basis of prior knowledge of the intragroup variation of tumour growth and immunotherapy treatment. Group sizes of 5–10 mice per genotype or treatment are commonly used in similar studies in the literature. These sample sizes are sufficient for determining statistical significance between groups and minimizing the number of animals or replicates needed for each experiment.
Data exclusions	No data were excluded.
Replication	Replicates were employed in all experiments, as explicitly stated in the text, figure legends and Methods.
Randomization	All mice and cells were randomized into experimental groups.
Blinding	The mice were selected randomly for tumour injection. Blinding was not implemented due to the necessity of case labeling and staffing requirements. Knowledge of the grouping information was essential for conducting the studies.

Reporting for specific materials, systems and methods

We require information from authors about some types of materials, experimental systems and methods used in many studies. Here, indicate whether each material, system or method listed is relevant to your study. If you are not sure if a list item applies to your research, read the appropriate section before selecting a response.

Materials & experimental systems

n/a	Involved in the study
☐	☒ Antibodies
☐	☒ Eukaryotic cell lines
☒	☐ Palaeontology and archaeology
☐	☒ Animals and other organisms
☒	☐ Clinical data
☒	☐ Dual use research of concern
☒	☐ Plants

Methods

n/a	Involved in the study
☒	☐ ChIP-seq
☐	☒ Flow cytometry
☒	☐ MRI-based neuroimaging

Antibodies

Antibodies used

For flow cytometry, anti-CD3 (317314, OKT3, BioLegend), anti-PD-1 antibody (329906, EH12.2H7, BioLegend), anti-LAG-3 antibody (46-2239-42, 3DS223H, Thermo), anti-EGFR antibody (352905, AY13, BioLegend), and anti-CD276 antibody (1188-MM06-F, Monoclonal Mouse IgG2b Clone #06, SinoBio), anti-Myc-tag antibody (2233S, 9B11, Cell Signaling Technology), anti-mCD3 antibody (1100312, 45-2C11, BioLegend), anti-Thy1.1 antibody (202522, OX-7, Biolegend).
For WB, anti-Myc tag antibody (2276S, 9B11, Cell signaling technology), anti-GAPDH antibody (60004-1-Ig, 1E6D9, Proteintech), anti-ATP1A1 antibody (14418-1-AP, Polyclonal, Proteintech), anti-EGFR antibody (2232, Polyclonal, Cell signaling technology) and anti-CD276 antibody (ab134161, EPNCIR122, Abcam), anti-CD3-ζ antibody (12837-2-AP, Proteintech) or an anti-pY142 CD3-ζ antibody (ab68235, Abcam).

Validation

All antibodies for FACS and WB were well-recognized clones in the field and validated by the manufacturers.

Eukaryotic cell lines

Policy information about cell lines and Sex and Gender in Research

Cell line source(s)

HEK293T cells were purchased from American Type Culture Collection (ATCC, Cat #CRL-3216). The cell lines GSC3565, GSC468 and GL261 were generated in our laboratory. The cell lines MGG4 and MGG6 were a kind gift from Dr. Hiroaki Wakimoto provided with a material transfer agreement from Massachusetts General Hospital. Glioblastoma primary cells were obtained from excess surgical resection samples from patients at The Second Affiliated Hospital Zhejiang University School of Medicine with appropriate consent and in accordance with an IRB-approved protocol (NO. IR2022453). Peripheral blood mononuclear cells (PBMCs) from healthy donors were purchased from Sailybio (China). The cell line NSC11 is a human neural stem cell line that was purchased from Alstem (hNSC11, Alstem). The HUVEC was purchased from ZQXZBIO (DFSC-EC-01, ZQXZBIO) and cultured in relevant culture medium (ZQ-1304, ZQXZBIO). Astrocytes and neural progenitor cells (NPCs) were differentiated from healthy donor-derived iPSCs following previously published protocols.

Authentication

All cell lines were routinely subjected to STR testing to confirm their identity.

Mycoplasma contamination

All cell lines tested negative for mycoplasma contamination.

Commonly misidentified lines
(See ICLAC register)

None of the cell lines used are listed in the ICLAC database.

Animals and other research organisms

Policy information about studies involving animals; ARRIVE guidelines recommended for reporting animal research, and Sex and Gender in Research

Laboratory animals

NOD/SCID/IL2Rg−/− (NSG) mice (005557, JAX Lab), C57BL/6J mice (000664, JAX Lab)

Wild animals

The study did not involve wild animals.

Reporting on sex

Sex was not considered in the study design.

Field-collected samples

The study did not involve samples collected from the field.

Ethics oversight

All mouse experiments were performed under an animal protocol approved by the Institutional Animal Care and Use Committee of Westlake University and in accordance with the relevant guidelines.

Note that full information on the approval of the study protocol must also be provided in the manuscript.

Flow Cytometry

Plots

Confirm that:

☒ The axis labels state the marker and fluorochrome used (e.g. CD4-FITC).

☒ The axis scales are clearly visible. Include numbers along axes only for bottom left plot of group (a 'group' is an analysis of identical markers).

☒ All plots are contour plots with outliers or pseudocolor plots.

☒ A numerical value for number of cells or percentage (with statistics) is provided.

Methodology

Sample preparation	All cell-line or tumor tissue samples were dissociated into single cells and stained as per the manufacturer's protocols before flow-cytometry assaying.
Instrument	CytoFLEX LX (Beckman Coulter)
Software	CytoFlEX LX software was used for data collection. FlowJo v.10 software was used for analysis.
Cell population abundance	No post-sort analysis was done on sorted cell populations from CAR T cells processed immediately for bulk RNA-seq and single cell RNA-seq.
Gating strategy	All gates were set based on isotype control antibodies after appropriate compensation using single-stained compensation controls.

☒ Tick this box to confirm that a figure exemplifying the gating strategy is provided in the Supplementary Information.